Effect of point defects and lattice distortions on the structural, electronic, and magnetic properties of Co_2MnAl Heusler alloy

Amar Kumar [1], Sujeet Chaudhary [1,*] and Sharat Chandra [2,†]

[1]*Thin Film Laboratory, Department of Physics, Indian Institute of Technology Delhi, New Delhi-110016, India*

[2]*Material Science Group, Indira Gandhi Centre for Atomic Research, Homi Bhabha National Institute (HBNI), Kalpakkam, Tamil Nadu-603102, India*

(Received 6 January 2024; revised 16 February 2024; accepted 27 February 2024; published 18 March 2024)

The effects of various point defects and lattice distortions have been studied on the structural, electronic, and magnetic properties of the Co_2MnAl alloy, considering the thermodynamically feasible range for the disorder concentrations. The Al_{Mn} binary antisite-disordered structures ($Co_2Mn_{0.9375}Al_{1.0625}$ and $Co_2Mn_{0.875}Al_{1.125}$) and ($Co_{Mn} + Al_{Mn}$)-ternary antisite-disordered structure ($Co_{2.0625}Mn_{0.875}Al_{1.0625}$) may be formed spontaneously during the synthesis of Co_2MnAl due to their negative relative formation energies. The Al-deficient structures resulting from Co_{Al} and Mn_{Al} binary antisite disorder ($Co_{2.0625}MnAl_{0.9375}$, $Co_{2.125}MnAl_{0.875}$, $Co_2Mn_{1.0625}Al_{0.9375}$, and $Co_2Mn_{1.125}Al_{0.875}$) and from ($Co_{Al} + Mn_{Al}$)-ternary antisite disorder ($Co_{2.0625}Mn_{1.0625}Al_{0.875}$) exhibit perfect half-metallicity. All other antisite disorders have a marginal effect on the half-metallic properties, and the disordered Co_2MnAl maintains the high spin polarization ($\geqslant 70\%$) along with nearly the same magnetization as the $L2_1$-ordered structure. Conversely, vacancy defects seriously affect the electronic and magnetic properties with rapid shrinking of the minority pseudogap. Also, the effect of vacancy occurrence on the structural, electronic, and magnetic properties is found to be very susceptible to their concentrations. For lattice distortions, the uniform strain ($\Delta V/V_0$) has a minimal effect on spin polarization and magnetization. Under negative strain within the range $-10\% \leqslant \Delta V/V_0 \leqslant 7\%$ (for $5.50\,\text{Å} \leqslant a \leqslant 5.58\,\text{Å}$), the strained structures showed perfect half-metallicity. For uniform strain $>7\%$, spin polarization decreases monotonically; however, it remains high, reaching $\sim 60\%$ at $\Delta V/V_0 = 10\%$ ($a = 5.88\,\text{Å}$). Contrarily, the tetragonal distortions, except for small distortion values ($\Delta c/a \leqslant\sim \pm 0.10$), lead to significant degradation in half-metallic behavior. Moreover, the elongation along the c axis (with compression of the ab plane) is found to be the favored condition for the occurrence of tetragonal distortion over compression along the c axis (with elongation of the ab plane). Thus, the resulting perfect half-metallicity in disordered Co_2MnAl suggests that the occurrence of disorder could also be beneficial sometimes for spintronic applications.

DOI: 10.1103/PhysRevMaterials.8.034405

I. INTRODUCTION

Materials with high spin polarization (P) and high Curie temperature (T_c) are promising for spintronic applications. Full Heusler alloys (HAs) containing Co and Mn as transition metal elements, such as Co_2MnZ with Z as an sp-group element, have been theoretically predicted and experimentally demonstrated to be attractive candidates for spintronic applications due to their remarkable properties, specifically very high spin polarization ($\sim 100\%$, theoretically), high Curie temperature, low saturation magnetization, and structural compatibility with conventional wide-gap semiconductors. In Co_2MnZ HAs, the presence of Co and Mn atoms ensures high T_c and high P at the Fermi level, respectively [1,2]. Although there are many reports for 100% spin polarization in HAs with perfectly ordered structures from the band structure calculations, most of the measurements of spin polarization in HAs yield only modest values, typically ranging from 40% to 50%; which leads to the poor performance of spintronic devices. However, the recent observation of $\sim 100\%$ spin polarization in $L2_1$-ordered epitaxial thin films of Co_2MnSi demonstrates that, with controlled growth conditions, even $\sim 100\%$ spin polarization is achievable experimentally for HAs [3]. Numerous experimental and theoretical studies have indicated that the structural imperfections originating from various point defects and lattice distortions are the prominent reasons for the experimentally observed low spin polarization of HAs. The experimentally synthesized HA thin films are often prone to various point defects and lattice distortions; for example, atomic swap disorder between Fe and Al atoms in the Co_2FeAl alloy [4], Co vacancy in the Co_2TiSb alloy [5], antisite disorder between Mn-Ga sites in the Mn_2NiGa alloy [6], and meta-stable tetragonal phase formation in Mn_2CoAl upon Ar^+ irradiation [7]. Thus, the presence of point defects and lattice distortions within HAs thin films can be considered a common occurrence.

In general, point defects in the HAs thin film can be categorized into five major categories: site disorder, antisite disorder, vacancy defects, interstitial defects, and impurity defects. Among these, site disorder, antisite disorder, and va-

*sujeetc@iitd.ac.in
†sharat@igcar.gov.in

cancy defects are the most commonly observed point defects in Co-based full HAs. The presence of other point defects, like interstitials and impurity defects, has rarely been reported in the literature [8]. The presence of all these structural imperfections in thin films is primarily dictated by the growth conditions, especially thermodynamic conditions for growth. Many recent studies have inferred that the presence of various point defects typically leads to the degradation of the half-metallic properties of HAs. However, a few material-specific defects can also coexist where the half-metallic nature and magnetization of HAs remain nearly the same. Recently, Rani *et al.* [9] found antisite disorder among Fe-Si sites and Cr-Si sites in the $Co_2Fe_{1-x}Cr_xSi$ alloy ($x = 0$, 0.125, 0.25, 0.50, and 1.00) using extended x-ray absorption fine structure (EXAFS) studies; this disorder leads to a reduction in total magnetization for the disordered structures. The presence of 5% antisite disorder between Ga-V sites in the FeMnVGa quaternary alloy has been experimentally detected by EXAFS and ^{57}Fe-Mossbauer spectrometry. Subsequently, by utilizing density functional theory (DFT) calculations, it was revealed that this disorder resulted in a decrease in spin polarization from 90% to 81% [10]. Using DFT calculations, Enamullah *et al.* [11] anticipated that antisite disorder between Co-Cr and Cr-Al sites in the CoMnCrAl alloy and between Co-Cr sites in the CoFeCrGe alloy should be observed experimentally due to their exceptionally low negative formation energies. Also, these antisite disorders induce a transition from a half-metallic to a metallic state, which is accompanied by a reduction in total magnetization. In another study, Enamullah *et al.* [12] investigated the impact of binary and ternary antisite disorders on the electronic properties of the Co_2MnSb alloy using first-principal methods. In that study, Co_2MnSb was found to be tolerant to low levels of disorder and retained its half-metallic behavior for small concentrations of various antisite disorders. However, as the degree of antisite disorders among the different transition metal elements is increased, a transition from a half-metallic to a metallic state occurs, except for the Co-Mn sites and Mn-Sb antisite disorders which, however, retain half-metallic nature and perfect magnetization even at high disorder concentrations of 11.25%. They found that Mn-excess antisite defects have the maximum probability of occurrence during experimental synthesis. Therefore, based on these studies, it can be inferred that the presence of atomic disorder significantly alters the electronic and magnetic properties, depending on both the material under study and the type of disorder. Thus, understanding the effect of various point defects on the structural, electronic, and magnetic properties of HAs is crucial for spintronics.

On the other hand, lattice distortions in HA thin films generally occur either uniformly, tetragonally, or octahedrally. These distortions can occur due to various factors such as lattice mismatch with the substrate or adjacent buffer layer, thermal treatment of the deposited film, or specific deposition technique employed. In most cases, lattice mismatch with adjacent layers leads to uniform (i.e., isotropic) strain or tetragonal (i.e., anisotropic) distortion in the HA thin film. For spintronic applications, for example, Co_2MnAl (lattice parameter, $a = 5.70$ Å) might be required to be deposited on Si substrate ($a = 5.43$Å) and/or MgO substrate ($a = 4.25$ Å), resulting in tetragonal distortion of the HA lattice [13,14]. Furthermore, the thermal treatment process, utilized for improving the microstructure of the deposited films during or after growth, significantly affects the lattice parameters of the deposited films and usually leaves the uniformly expanded lattice (or uniform tensile strain) [15–18]. The thin films prepared by the sputter techniques may have stress of ± 1 GPa because of the preparation method alone [19–22]. Such substantial stress generally results in uniform tensile or compressive strain in the lattice. All these distortions can significantly modify the structural, electronic, and magnetic properties of HAs. For instance, in the Co_2FeAl alloy, 100% spin polarization is retained under 0 to +4% uniform strain (defined with respect to the optimized lattice parameter), while it decreases from 90% to 16% for −1% to −6% negative strains. Also, Co_2FeAl is found to be very sensitive to tetragonal distortions, as 100% spin polarization is preserved only under cubic strain [23]. However, unlike the point defects, which often adversely affect material functionality for spintronics, the lattice deformation in HA thin films can also result in some advantageous phenomena. For instance, lattice deformations can increase the in-plane magnetic anisotropy due to large mismatches with adjacent layers [15,24]. Additionally, HAs with metastable or stable tetragonal phase can also have some useful phenomena like perpendicular magnetic anisotropy (PMA), intrinsic exchange bias, shape memory effect, magnetocaloric effect, and wide-ranging applications for sensors and actuators [25]. Therefore, a comprehensive study of the lattice distortion effects, including compressive- and tensile-uniform strain, as well as tetragonal distortion on the electronic and magnetic properties of HAs is also equally important. Additionally, the coexistence of a stable or metastable tetragonal phase alongside the cubic phase in HAs can provide significant potential and benefits.

Among Co_2MnZ full HAs, Co_2MnAl exhibits very high spin polarization of $\sim 76\%$ at the Fermi level (E_F), saturation magnetization (M_s) of $\sim 4.02\,\mu_B$/f.u., and high T_c of ~ 720 K, making it a promising candidate for spintronics. However, despite these promising characteristics, there are limited investigations regarding the effects of point defects and lattice distortions on the structural, electronic, and magnetic properties of the Co_2MnAl alloy. Galanakis *et al.* [26] have studied the impact of various point defects, such as antisite disorder between Mn-Al and Co-Mn sites, particularly Al_{Mn}, Mn_{Al}, and Mn_{Co}, and vacancies at Co, Mn, and Al sites (V_{Co}, V_{Mn}, and V_{Al}) using DFT calculations. Here, A_B antisite disorder is defined as the substitution of a B atom by an A atom, and V_X denotes a vacancy defect at the X atomic site in an ideal crystal. Both antisite disorders and vacancy defects lead to an off-stoichiometric alloy while maintaining the total number of atoms constant. They found that the presence of V_{Co}, V_{Mn}, and V_{Al} leads to the depolarization of Co_2MnAl, while Mn_{Co} has mild effect on the spin polarization. Regarding magnetization, total magnetic moment increases for Mn_{Al} antisite disorder, whereas it decreases for Al_{Mn} and Mn_{Co} antisite disorders.

More recently, Feng *et al.* [27] have studied the influence of Mn content on half-metallicity and magnetism of off-stoichiometric Co_2MnAl through DFT calculations. For Mn-rich structures, they considered Mn_{Co} and Mn_{Al} antisite disorders; and for Mn-poor structures, they studied Co_{Mn} and Al_{Mn} antisite disorders along with V_{Mn} vacancy defects.

Mn-rich samples resulting from Mn_{Co} antisite disorder and Mn-poor samples resulting from Co_{Mn} antisite disorder are expected to be experimentally observed due to their lower relative formation energies (RFEs). Density of states (DOS) calculations revealed that the presence of Co_{Mn} and Mn_{Co} antisite disorders led to decreased and increased P, respectively, while the presence of Al_{Mn} antisite disorder leaves P unchanged. As the concentration of Mn_{Co} disorder increases in the $Co_{2-x}Mn_{1+x}Al$ alloy, the disordered alloy exhibits 100% spin polarization from $x = 0.50$ to 0.875 and turns into a spin gapless semiconductor at $x = 1$, which is an exceptionally intriguing phenomenon. However, there is a lack of comprehensive studies that include all possible antisite disorders involving transition metal elements and *sp*-group elements as well as vacancy defects for various types of atoms. To the best of our knowledge, theoretical investigations of Co_2MnAl have not covered the Al_{Co} antisite disorder ($Co_{2-x}MnAl_{1+x}$) and ternary antisite disorder involving three atoms (i.e., $Co_{2+x+y}Mn_{1-x}Al_{1-y}$, $Co_{2-x}Mn_{1+x+y}Al_{1-y}$, and $Co_{2-x}Mn_{1-y}Al_{1+x+y}$). Notably, ternary antisite disorders are favored in experimental growth and have been observed extensively [28]. Also, the spin polarization and magnetization level in the presence of various vacancy defects are yet to be explored. Regarding the lattice distortion effects in Co_2MnAl, Nepal *et al.* [29] have explored the impact of lattice parameter variation on M_s of Co_2MnAl by changing the experimental lattice parameter (5.75 Å) by ±2%. They showed that a uniform expansion of the lattice by 2% (lattice parameter 5.86 Å) did not change the total magnetic moment from its ideal value ($\sim 4.12\,\mu_B$/f.u.). However, when the lattice is uniformly contracted by 2% (lattice parameter 5.63 Å), the total magnetic moment increased to $\sim 5.00\,\mu_B$/f.u. Under lattice distortion, the major change was observed in the magnetic moments of Mn atoms, whereas the magnetic moments of the Co atoms experienced minor modifications [29]. However, a comprehensive investigation of lattice distortion effects on Co_2MnAl is lacking; particularly, the impact of uniform strain and tetragonal distortion remains unexplored.

Interestingly, some reports have highlighted exceptional behaviors exhibited by Co_2MnAl in the presence of structural imperfections, such as enhanced spin polarization in the presence of B2-site disorder as compared with the $L2_1$-ordered structure reported by utilizing *ab initio* DFT calculations [30], emergence of high PMA in the presence of lattice distortions and antisite disorders demonstrated experimentally [31], and spin gapless semiconducting (SGS) nature in the presence of high disorder degree of Mn_{Co} antisite disorder observed experimentally [28] as well as employing DFT calculations [27]. Remarkably, such anomalous behaviors of Co_2MnAl in the presence of structural perturbations are rarely observed for other Co-based HAs. Given the partial availability of results for the effect of point defects and lattice distortions, such phenomenal occurrences in the presence of structural imperfections further motivate and emphasize the necessity of comprehensively exploring the effects of structural imperfections on the structural, electronic, and magnetic properties of Co_2MnAl alloy vis-à-vis the type of defects. Therefore, we have tried to systematically study the effect of various point defects (binary antisite disorder, ternary antisite disorder, and vacancy defects) and lattice distortions (uniform tensile strain, uniform compressive strain, and tetragonal distortion) on the structural, electronic, and magnetic properties of the Co_2MnAl alloy.

The rest of this paper is organized as follows: First, the computational methodology adopted for this paper is briefly discussed in Sec. II. Next, the validation of the exchange-correlation (XC) functional used for studying the physical properties of the Co_2MnAl alloy is discussed in Sec. III A. This is followed by the presentation of comprehensive results on the effect of the presence of various point defects (binary antisite, ternary antisite, and vacancy defects with different disorder concentrations) and lattice distortions (uniform strains and tetragonal distortions) on the structural, electronic, and magnetic properties of the Co_2MnAl alloy in Secs. III B and III C, respectively. Finally, a detailed summary of all the findings is provided in the concluding section (Sec. IV).

II. COMPUTATIONAL DETAILS

The pseudopotential plane-wave DFT calculations, as implemented in QUANTUM ESPRESSO, are carried out to study the effect of various point defects and lattice distortions on structural, electronic, and magnetic properties of Co_2MnAl HAs [32,33]. The generalized gradient approximation (GGA) and GGA + U method have been used to deal with the electronic exchange and correlation interactions, with U representing the Hubbard parameter within the linear-response method of Cococcioni [34]. The scalar relativistic projector augmented-wave pseudopotentials from PSlibrary with valence-electron configurations of Co ($3s^2\,3p^6\,4s^2\,3d^7$), Mn ($3s^2\,3p^6\,4s^2\,3d^5$), and Al ($3s^2\,3p^1$) are used to deal with electron-ion interaction correctly [35]. The validations of the XC functional for the Co_2MnAl alloy and the effect of lattice distortions on the structural, electronic, and magnetic properties of Co_2MnAl have been studied using a 16 atom unit cell, whereas for study of the effect of point defects on the structural, electronic, and magnetic properties of Co_2MnAl, a 64 atom supercell ($2 \times 2 \times 1$ supercell) has been used. For the 16 atom unit cell, an energy-converged Monkhorst-Pack $15 \times 15 \times 15$ k-point grid and plane-wave cutoff energy of 250 Ry are chosen for calculations. Accordingly, for the 64 atom supercell, a $7 \times 7 \times 15$ sized Monkhorst-Pack grid is used to maintain the same k-point density between the 16 and 64 atom unit cells. This causes a very small energy difference of <0.1 meV/f.u. in total energies between the 16 and 64 atom unit cells. The optimized tetrahedron method is employed to perform the Brillouin zone integration [36]. The convergence threshold for self-consistency is set to be 10^{-6} Ry. For lattice distortions, only atomic positions and for point defects, atomic positions along with the cell parameters (full-cell relaxation) are allowed to relax to find out the corresponding optimized structure, with a force convergence criteria of 10^{-3} Ry/bohr. As spin-orbit coupling has a minor effect on structural, electronic, and magnetic properties of Co_2Mn-based full HAs, this effect is not considered for the calculations [2].

III. RESULTS AND DISCUSSION

A. XC functional validation for Co_2MnAl

Numerous approximations exist for XC functionals, with the three primary being local density approximation (LDA),

TABLE I. The calculated Hubbard parameters (U_{Co} for Co atoms and U_{Mn} for Mn atoms), optimized lattice parameter a (Å), total magnetic moment M_s (μ_B/f.u.), atomic magnetic moments (m_{Co}, m_{Mn}, m_{Al} for Co, Mn, and Al atomic moments, respectively), and spin polarization (P) for $L2_1$-ordered Co_2MnAl with different XC functionals. The other theoretical and experimental results are also provided for comparison. Exp. denotes experimental data, and the lattice parameters marked with an asterisk (*) indicate that the fixed experimental lattice parameter (i.e., 5.75 Å) is used for calculating the electronic and magnetic properties.

Properties	This paper (GGA)	This paper (GGA + U)	Tsirogiannis *et al.* [37] (GGA + U)	Nepal *et al.* [29] (GGA + U)	Webster *et al.* [38] (Exp.)	Guillemard *et. al.* [39] (Exp.)
U_{Co} (eV)	–	5.93	2.70	2.70	–	–
U_{Mn} (eV)	–	4.40	3.65	3.65	–	–
a (Å)	5.69	6.23	5.75*	5.75*	5.75	5.76
M_s (μ_B/f.u.)	4.02	7.25	6.44	4.86	4.01	4.32
m_{Co} (μ_B)	0.80	1.54	1.38	0.87	0.50	–
m_{Mn} (μ_B)	2.59	4.29	4.18	3.43	3.01	–
m_{Al} (μ_B)	−0.07	–	–	–	–	–
P	76.16%	80.71%	–	–	–	63%

GGA, and hybrid functionals. The accuracy of DFT calculations strongly depends upon the approximation used for the XC functional. To ensure that the chosen XC does not influence the outcomes, we first benchmarked the adequate XC functional for the Co_2MnAl alloy. Hybrid functionals are well known for accurately describing a wide range of electronic properties like lattice parameters, magnetic moments, and electronic band gaps. However, they require very high computational costs due to the incorporation of nonlocal potential. Therefore, a hybrid XC functional is not used for calculations. The GGA XC approximates almost accurately the structural, electronic, and magnetic properties of a metallic system compared with LDA; therefore, we have calculated these properties of Co_2MnAl using the GGA XC functional.

Moreover, as Co_2MnAl contains the 3d-transition elements (Co and Mn), accounting for the on-site Coulomb repulsion between the localized d electrons is needed for better predictions of electronic properties. Therefore, the Hubbard U correction is incorporated with the GGA functional for DFT calculations. Here, U represents the on-site Coulomb potential, which can also be understood as an add-on to the GGA XC. The U values are calculated using the linear-response method of Cococcioni [34]. The calculated Hubbard parameter (U) for the Co and Mn atoms is 5.93 and 4.41 eV, respectively, falling well within the typical range observed for U values of most 3d-transition elements (between 1 and 5 eV). The calculated DOS plots without and with the specified U values are given in Figs. S1(a) and S1(b) in the Supplemental Material [35], respectively. At once, the calculated U values might appear relatively large compared with the reported values of 2.5–3.5 eV for Co and Mn atoms for Co- and Mn-based HAs [36], but it is important to note that the U values depend on several factors, such as calculation method, choice of potentials, and basis set. Thus, they are not fixed constants and can have different values with different inputs for the same element. The calculated optimized lattice parameter a (Å), total magnetic moment M_s (μ_B/f.u.), atomic magnetic moment (m_X), and spin polarization (P) using the GGA and GGA + U methods, with the obtained U values, are presented in Table I along with other results wherever available. As seen from Table I, the calculated parameters using the GGA + U method significantly exceed the experimental and GGA findings. In contrast, the results obtained using GGA are consistent with the experimental results. Therefore, the GGA + U method with specified U values is not beneficial for Co_2MnAl, and GGA proves to be an adequate XC for studying the electronic properties of Co_2MnAl. This observation is also consistent with the other available GGA + U studies for Co_2MnAl so far, which further supports the validation of the incompatibilities of the GGA + U method to study the electronic properties of the Co_2MnAl alloy [30,37,40]. Therefore, the GGA XC would be used for further calculations.

B. Effect of point defects on structural, electronic, and magnetic properties of Co_2MnAl

In this section, the effect of various point defects, namely, binary antisite disorders, ternary antisite disorders, and vacancy defects, on the structural, electronic, and magnetic properties of Co_2MnAl using an 16 f.u. unit cell (i.e., 64 atom supercell) is discussed. For binary antisite disorders, the Co_{Mn} antisite ($Co_{2+x}Mn_{1-x}Al$), Co_{Al} antisite ($Co_{2+x}MnAl_{1-x}$), Mn_{Co} antisite ($Co_{2-x}Mn_{1+x}Al$), Mn_{Al} antisite ($Co_2Mn_{1+x}Al_{1-x}$), Al_{Co} antisite ($Co_{2-x}MnAl_{1+x}$,) and Al_{Mn} antisite ($Co_2Mn_{1-x}Al_{1+x}$) have been considered. Since in experiments the atomic vacancy can occur at any atomic site, the monovacancies and divacancies for the Co atomic site ($Co_{2-x}MnAl$ or V_{Co}), Mn atomic site ($Co_2Mn_{1-x}Al$ or V_{Mn}), and Al atomic site (Co_2MnAl_{1-x} or V_{Al}) have been examined. For ternary antisite disorder, ($Mn_{Co} + Al_{Co}$)-antisite disorder ($Co_{2-2x}Mn_{1+x}Al_{1+x}$ or Co-deficient structure), ($Co_{Mn} + Al_{Mn}$)-antisite disorder ($Co_{2+x}Mn_{1-2x}Al_{1+x}$ or Mn-deficient structure), and ($Co_{Al} + Mn_{Al}$)-antisite disorder ($Co_{2+x}Mn_{1+x}Al_{1-2x}$ or Al-deficient structure) have been reviewed. The value of x, which is directly connected to the disorder concentration through the number of substituted atoms, is taken as 0.0625 and 0.125 for modeling the binary antisite disorders and vacancy defects, whereas the ternary antisite disorders have been modeled using $x = 0.0625$.

The value of x is chosen considering the following facts: As reported in the literature, a high disorder concentration of the antisite disorders and vacancy defects typically results in very high positive or negative RFEs for the defected structure. For the significantly high positive RFEs, defects are easily remov-

able via high-temperature processing, viz., high-temperature thin film growth and/or postdeposition annealing. Conversely, exceedingly negative RFEs at high concentrations can lead to phase separation [41,42]. Additionally, detecting very small disorder concentrations using conventional experimental techniques presents a challenge [43]. For this reason, in most experiments where the occurrence of antisite disorders and vacancy defects have been reported, the disorder concentrations range varies from 5% to 15%. For example, $\sim 5\%$ of the Co sites are occupied by Mn atoms, and 14% of the Mn sites are occupied by Co atoms in the Co_2MnSi alloy [44]; 10% antisite disorder between Ti-Al sites in the Co_2TiAl alloy [45]; 16% antisite disorder between Fe-Al sites in the Co_2FeAl alloy [46]; and 13% of the Ga sites are occupied by Mn atoms in the Mn_2NiGa alloy [6]. Therefore, we have tried to study the antisite disorders and vacancy defects with a degree of disorder (or disorder concentration or defect concentration) ranging from 3.125% to 12.50%. Here, the degree of disorder (or degree of defect) is defined as the ratio of the number of substituted atoms (also referred to as replaced atoms) to the total number of the same kind of atoms within a 64 atom supercell. Therefore, when the x value is chosen as 0.0625 and 0.125, the disorder concentrations are 6.25% and 12.50%, respectively, for Co_{Mn}, Co_{Al}, Mn_{Al}, Al_{Mn}, V_{Mn}, and V_{Al} disorders. For Mn_{Co}, Al_{Co}, and V_{Co} disorders, the x values of 0.0625 and 0.125 correspond to the disorder concentrations of 3.125% and 6.25%, respectively. Notably, for the Mn_{Co}, Al_{Co}, and V_{Co} defects, the disorder degree of 9.375% (corresponding to disorder at 3 Co atomic sites out of a total 32 Co atomic sites) and 12.50% (corresponding to disorder at 4 Co atomic sites out of a total 32 Co atomic sites) have been ignored due to limitations in computational resources. Also, for the ternary antisite disorder, the higher disorder concentrations (high values of x) have not been considered for the same reason.

Since describing the disordered structures in terms of x values appears to be a more convenient and flexible approach, we will continue to use these specific x values to specify disorder concentration unless otherwise stated for a particular case. Prior to evaluating the physical properties of a specific disordered structure, all possible atomic configurations for corresponding disorder concentration are considered using the supercell approach, and the full-cell relaxations were performed to identify the most stable atomic configuration (with the lowest total energy) for that specific disorder concentration. After that, the structural, electronic, and magnetic properties of that specific disordered structure are calculated using the most stable atomic configuration. The full-cell relaxation calculations also reveal that changes in lattice parameters and atomic positions are $<1\%$ for all disordered structures. Therefore, it can be concluded that the disorder leaves the cell structure unchanged. In the following subsections, we will first discuss the formation energy, then spin polarization, and finally, the magnetic moments for the point defects.

1. Formation energy of the point defects

The formation energy provides information about the ease of occurrence of the disorder (i.e., the order in which it can form during the experimental growth) as well as the relative thermodynamic stability of the disordered structures. Therefore, the RFEs for the point defects with respect to $L2_1$-ordered structure, or simply referred to as the defect formation energy sometimes, have been calculated to find out the possibility of defect formation, using the following formula:

$$E_{\text{form}}(X) = E_{\text{tot}}(X) - E_{\text{tot}}(L2_1) - \sum_i n_i \mu_i, \tag{1}$$

where $E_{\text{form}}(X)$ and $E_{\text{tot}}(X)$ represent the RFE and total energy for the defected structure (X), respectively, and $E_{\text{tot}}(L2_1)$ is the total energy for the fully ordered Co_2MnAl alloy (i.e., $L2_1$ structure) in the equivalent cell. Here, n_i is $+1$ (-1) for an excess (deficiency) of atom of species i, and μ_i is the chemical potential of the corresponding element. The μ_i for the constituting elements is taken as the ground-state energy of the corresponding atoms in their bulk stable form: hexagonal close-packed–ferromagnetic Co, [001] face-centered cubic (fcc)-antiferromagnetic Mn, and fcc-nonmagnetic Al. The competing crystalline phases and charge defects that might form during defective growth are not considered. The calculated RFE using Eq. (1) for binary antisite disorders and vacancy defects are given in Table II, while those for ternary antisite disorders are listed in Table III. The negative RFE for the defected structure suggests that such defect formation is accompanied by energy release, making them likely to form spontaneously during the experimental growth. Conversely, the positive RFE for the defected structure implies that the defected structure may be formed by absorbing energy and therefore is less likely to form during the growth of Co_2MnAl. In general, a much higher positive RFE implies that the synthesis of the defect would be less favorable in the experiments. Furthermore, at the thermodynamic equilibrium, the equilibrium concentration of a defect at temperature T can be approximated using RFE with the following equation [47,48]:

$$D_{\text{def}} = N_{\text{sites}} N_{\text{config}} \exp\left(-\frac{E_{\text{form}}}{kT}\right). \tag{2}$$

Here, N_{sites} and N_{config} are the number of available sites and equivalent configurations where the defect can be incorporated. However, using Eq. (2), only a qualitative estimate of the defect concentration is possible, as Eq. (2) is strictly valid in the limit of very low concentrations and greatly exceeds when considering more than a few percent.

For the binary antisite disorders and vacancy defects with $x = 0.0625$, RFE is positive except for Al_{Mn} antisite disorder. The Al_{Mn} antisite disorder has negative RFE; therefore, Al_{Mn} disorder is most likely to be formed during the experimental growth of Co_2MnAl, and it is supposed to be formed spontaneously, as suggested by Eq. (2). For all other cases, the decreasing order for the probability of formation is as follows: Mn_{Co}, Al_{Co}, Co_{Mn}, Mn_{Al}, Co_{Al}, V_{Co}, V_{Mn}, and V_{Al}. Although, the Co_{Al} antisite and V_{Co}, V_{Mn}, and V_{Al} vacancy-defected structures have very high positive RFE, their occurrence cannot be excluded. They are expected to survive with a small density according to Eq. (2). While increasing the disorder concentration, i.e., with $x = 0.125$, the RFE nearly doubles for all cases. Such changes in RFE are naturally established here due to the almost localized and isolated nature of disorders, which will be discussed later in Secs. III B 2 and

TABLE II. The different disorders along with resulting structure nature; RFE, spin polarization, and minority spin band gap values for binary antisite-disordered and vacancy-defected structures.

Disorder type	x	Stoichiometric formula	RFE (eV)	Spin polarization P (%)	Minority spin band gap (eV)
$L2_1$ order	–	Co_2MnAl	–	76.13	0.66
Co_{Mn} antisite	0.0625	$Co_{2.0625}Mn_{0.9375}Al$	0.56	71.56	–
$(Co_{2+x}Mn_{1-x}Al)$	0.1250	$Co_{2.125}Mn_{0.875}Al$	1.13	67.64	–
Co_{Al} antisite	0.0625	$Co_{2.0625}MnAl_{0.9375}$	1.68	100.00	0.17
$(Co_{2+x}MnAl_{1-x})$	0.1250	$Co_{2.125}MnAl_{0.875}$	3.38	100.00	0.19
Mn_{Co} antisite	0.0625	$Co_{1.9375}Mn_{1.0625}Al$	0.24	86.73	0.37
$(Co_{2-x}Mn_{1+x}Al)$	0.1250	$Co_{1.875}Mn_{1.125}Al$	0.48	88.23	0.37
Mn_{Al} antisite	0.0625	$Co_2Mn_{1.0625}Al_{0.9375}$	1.28	100.00	0.72
$(Co_2Mn_{1+x}Al_{1-x})$	0.1250	$Co_2Mn_{1.125}Al_{0.875}$	2.53	100.00	0.63
Al_{Co} antisite	0.0625	$Co_{1.9375}MnAl_{1.0625}$	0.41	83.76	0.64
$(Co_{2-x}MnAl_{1+x})$	0.1250	$Co_{1.875}MnAl_{1.125}$	0.80	75.53	0.63
Al_{Mn} antisite	0.0625	$Co_2Mn_{0.9375}Al_{1.0625}$	−0.67	71.56	0.55
$(Co_2Mn_{1-x}Al_{1+x})$	0.1250	$Co_2Mn_{0.875}Al_{1.125}$	−1.41	87.14	0.24
Co vacancy	0.0625	$Co_{1.9375}MnAl$	1.68	60.19	–
$(Co_{2-x}MnAl)$	0.1250	$Co_{1.875}MnAl$	3.01	69.08	–
Mn vacancy	0.0625	$Co_2Mn_{0.9375}Al$	3.04	54.04	–
$(Co_2Mn_{1-x}Al)$	0.1250	$Co_2Mn_{0.875}Al$	5.72	25.60	–
Al vacancy	0.0625	$Co_2MnAl_{0.9375}$	4.07	83.31	0.52
(Co_2MnAl_{1-x})	0.1250	$Co_2MnAl_{0.875}$	7.87	80.72	0.43

III B 3. These results for RFE exhibit a similar trend for the cases that have been studied in Ref. [27] for Co_2MnAl. They are also consistent with the other first-principles findings for the Co_2MnSi alloy [49], where Si is analogous to Al in the Co_2MnAl alloy.

Regarding ternary antisite disorders, the Mn-deficient structure resulting from $(Co_{Mn} + Al_{Mn})$-antisite disorder exhibits negative RFE; therefore, it is likely to be formed spontaneously during experimental growth of Co_2MnAl, like Al_{Mn} antisite disorder. Meanwhile, the Co-deficient structure resulting from $(Mn_{Co} + Al_{Co})$-antisite disorder, and Al-deficient structure resulting from $(Co_{Al} + Mn_{Al})$-antisite disorder have moderate and very high RFE, respectively. Consequently, the likelihood of the occurrence is significantly reduced for the Co-deficient structure and almost negligible for the Al-deficient structure. As noted from Tables II and III, the RFE of the ternary antisite disorder can be approximated by summing the RFE of the individual binary antisite involved, which is the direct signature of isolation of binary antisite disorder (significant distance between both substituted atoms) inside the energetically favored ternary antisite disorder structure within the 64 atom supercell. Therefore, like binary antisite disorder, the effect of ternary antisite disorder should also be localized.

When considering the formation of various disorders, it is essential to note that the RFE values listed in Tables II and III are computed by considering the constituent atoms in their bulk stable form (under host-rich conditions), at absolute zero temperature and at absolute zero pressure. However, a similar qualitative behavior (order of formation) should be observed under realistic experimental thermodynamic conditions (i.e., at nonzero temperature and pressure), due to a linear change in RFE with nearly the same slope with respect to the chemical potential. It is

TABLE III. The different ternary antisite disorders along with the resulting structure nature; corresponding stoichiometric formula, RFE, spin polarization, and minority spin band gap values for the ternary antisite-disordered structures.

Disorder type	Structure nature	x	Stoichiometric formula	RFE (eV)	Spin polarization P (%)	Minority spin band gap (eV)
$Mn_{Co} + Al_{Co}$ $(Co_{2-2x}Mn_{1+x}Al_{1+x})$	Co-deficient	0.0625	$Co_{1.875}Mn_{1.0625}Al_{1.0625}$	0.60	84.50	0.52
$Co_{Mn} + Al_{Mn}$ $(Co_{2+x}Mn_{1-2x}Al_{1+x})$	Mn-deficient	0.0625	$Co_{2.0625}Mn_{0.875}Al_{1.0625}$	−0.10	66.99	–
$Co_{Al} + Mn_{Al}$ $(Co_{2+x}Mn_{1+x}Al_{1-2x})$	Al-deficient	0.0625	$Co_{2.0625}Mn_{1.0625}Al_{0.875}$	2.75	100.00	–

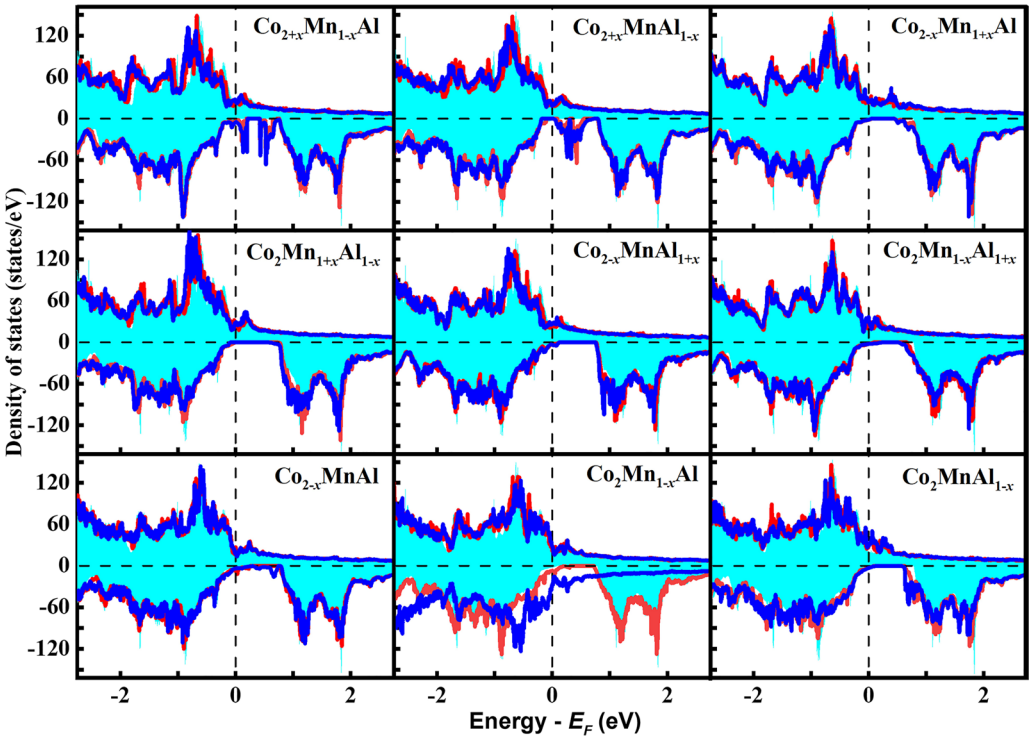

FIG. 1. Density of states (DOS) plots of various binary antisite-disordered and vacancy-defected structures. The shaded cyan area represents the DOS of ideal Co_2MnAl, while the solid red and blue lines represent DOSs for $x = 0.0625$ and 0.125, respectively. For the disordered structure, the stochiometric formula is given in the insight of each graph.

also crucial to stress about the negative RFE for Al_{Mn} binary antisite-disordered structures ($Co_2Mn_{0.9375}Al_{1.0625}$ and $Co_2Mn_{0.875}Al_{1.125}$) and for ($Co_{Mn} + Al_{Mn}$)-ternary antisite-disordered structures ($Co_{2.0625}Mn_{0.875}Al_{1.0625}$). These negative values signify that these disordered structures are relatively more likely to be formed than the pure crystalline system during the growth of Co_2MnAl, as also supported by Eq. (2). However, there is still a lack of control over the thermodynamics for the growth process and of the well-defined experimental method to probe such defects. For such cases, the formation of the mixed phase due to antisite disorder has been reported for many HAs [50,51]. To resolve this question unambiguously, advanced first-principles calculations are necessary, like in Ref. [42] or the *ab initio* atomistic thermodynamic calculations, which are beyond the scope of this paper [42].

2. *Effect of point defects on the electronic properties of* Co_2MnAl

Next, we pay attention to the effects of point defects (i.e., binary antisite disorders, vacancy defects, and ternary antisite disorders) on the electronic properties of the Co_2MnAl alloy. Before describing the influence of the point defects on the electronic properties, let us first discuss some important features of the DOS of the ideal (or $L2_1$ ordered) Co_2MnAl alloy. Like the DOS plot for other Co-based full HAs [52], the DOS plot of Co_2MnAl exhibits the peak and valley characteristics resulting from the d-orbital localization and van Hove singularities, as seen in Fig. S1(a) in the Supplemental Material [35]. The E_F lies in the spin valley for the majority spin channel (or the spin-up channel) and in the pseudogap for the minority spin channel (or the spin-down channel). As a result, Co_2MnAl is not a perfect half-metal; instead, it has a very high spin polarization of $\sim 76.13\%$ with nearly half-metallic characteristics. Co_2MnAl has a wide minority spin energy gap or the Slater-Pauling (SP) valley of 0.66 eV, located just above E_F. The origin of this minority gap has already been discussed in detail in the literature and is understood to be associated with the covalent hybridization between transition metal elements.

To study the impact of disorder on the electronic properties, the total DOS of the disordered structures is compared with the ideal case. In the presence of point defects, the majority channel DOS remains nearly the same as the $L2_1$-ordered structure, and the changes happen in the minority spin channel only near E_F, as depicted in Figs. 1 and 2. The extent of these changes depends on the specific type of disorder. For most of the considered disordered structures, with minor changes, the SP valley in the minority is nearly unscathed. However, in some cases, substantial modifications have also occurred in the minority DOS, including the emergence of new states in the minority spin channel. In addition to this, the minority gap width ($E_c - E_v$) also changes significantly for all disorders (see Tables II and III), while the Fermi energy (equivalently change in the minority gap center $\{(E_c + E_v)/2\}$ or shifting in SP valley) experiences minor but important modifications (Tables S1 and S2 in the Supplemental Material [35]). Here, E_c and E_v represent the minority valence band edge and minority conduction band edge near E_F. These alterations in the DOS plots can be attributed to a multitude of factors. The reason that the changes happened only in the minority spin channel of the ideal DOS, after incorporating the disorder,

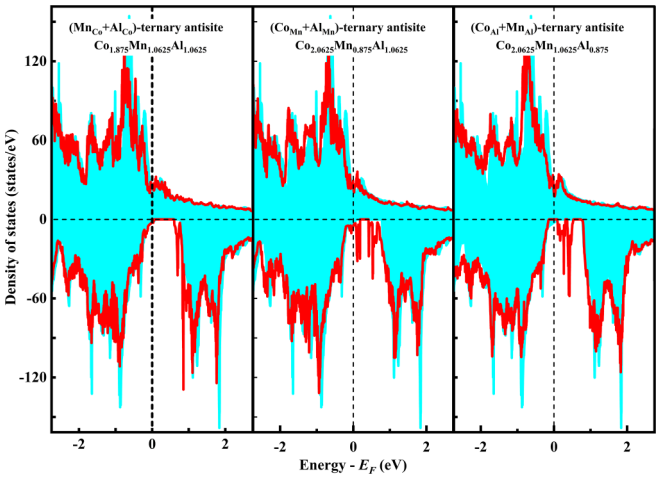

FIG. 2. Density of states (DOS) plots of various ternary antisite-disordered structures. The shaded cyan area represents the DOS of ideal Co_2MnAl, while the solid red is for $x = 0.0625$. For the disordered structure, the stochiometric formula is given insight of each graph.

can be explained as a step to minimize the band energy of the disordered structure, as discussed by Faleev *et al.* [52] for similar HAs. Further, the changes in the minority gap width, Fermi energy, and the emergence of new states in the minority spin channel appear from the changes in the hybridization between the constituting atoms of the disordered structures.

After that, the spin polarization for the disordered structures is determined using the formula $P = (D_1 - D_2)/(D_1 + D_2)$, where D_1 and D_2 represent the spin-up and spin-down DOSs at E_F, respectively. The alternations in DOS, as discussed above, lead to changes in P for the disordered structure. The calculated P and minority spin gap (real gap for structures having 100% spin polarization and pseudo-gap for others) for the binary antisite-disordered structures, vacancy-defected structures, and ternary antisite-disordered structures are listed in Tables II and III. Both binary and ternary antisite-disordered structures exhibit relatively high P (compared with the ordered structure). On the other hand, for the vacancy-defected structures (except the Al vacancies), a significant reduction in P is observed.

For binary antisite disorders and vacancy defects with the disorder concertation of $x = 0.0625$, minor modifications in DOS are observed for the Mn-rich structures (Mn_{Co} and Mn_{Al} antisite), Al-rich structures (Al_{Co} and Al_{Mn} antisite), and Al monovacancy, which can be described in terms of changes in the minority gap width and the shifting of the SP valley toward the high binding energies (Fig. 1). As a result, due to the presence of the smaller number of minority DOSs at E_F as compared with the ideal case, an increment in P is observed for these disordered structures. Remarkably, for the Mn_{Al} disordered structure, the absence of the minority spin states at E_F results in a perfectly half-metallic nature. Additionally, the Mn_{Al} disordered structure possesses a wide minority energy gap of 0.72 eV, even larger than the $L2_1$-ordered structure, making the Mn_{Al} disordered structure more suitable than the $L2_1$-ordered structure for spintronic applications. Meanwhile, in the case of Co-rich structures (Co_{Al} and Co_{Mn} antisite), V_{Co}, and V_{Mn}, significant alternations in DOS are observed along with the arising of the new bands within the minority gap. For the Co_{Al} antisite disorder, this modification is such that E_F falls in the energy gap in minority spin, resulting in 100% spin polarization for the Co_{Al} disordered structure. In contrast, for the Co_{Mn} antisite disorder, the complete closing of the minority spin gap takes place; therefore, a slight reduction ($\sim 71.56\%$) in P is observed for the Co_{Mn} disordered structure. Similarly, for the Co and Mn monovacancy defects, the minority DOSs are substantially affected, leading to the formation of a continuous band. This band is more intense in the presence of the Mn monovacancy than the Co monovacancy, resulting in a large reduction in spin polarization ($\sim 54.04\%$) for the Mn monovacancy-defected structure.

Upon increasing the disorder concentration (i.e., for $x = 0.125$), Mn_{Al} and Co_{Al} antisite-disordered structures retain their half-metallic nature. On the other hand, for Mn_{Co} and Al_{Mn} antisite-disordered structures, P increased, whereas for Co_{Mn} and Al_{Co} antisite-disordered structures, P is reduced. With the change in the disorder concentrations (i.e., from $x = 0.0625$ to 0.125), the minority band gap values for Mn_{Al} and Co_{Al} disordered structures changed to 0.63 and 0.19 eV, respectively, along with 100% P, making them beneficial even in the presence of disorder, especially in the case of Mn_{Al} disorder. For the case of divacancies (i.e., vacancy defects with $x = 0.125$), the impact is much more intense than for monovacancies. For Mn divacancy, the complete shrinking of the minority pseduogap takes place (see Fig. 1), leading to a large reduction in spin polarization ($\sim 25\%$). However, for the Co and Al divacancies, the effect on DOS and P is very similar to their monovacancies. Therefore, for Co and Al divacancies, spin polarization is nearly the same as that of monovacancies.

Next, for the ternary antisite disorders, DOS plots are given in Fig. 2. For the Co-deficient structures, there are marginal changes in the DOS shape. In contrast, for the Mn- and Al-deficient structures, the emergence of new states in the minority gap is accompanied by changes in the gap width and shifting of minority DOS (Fig. 2). In the Co-deficient structure [or ($Mn_{Co} + Al_{Co}$)-ternary disordered structure], reduced minority DOS at E_F leads to the enhancement in P. For the Al-deficient structure [or ($Co_{Al} + Mn_{Al}$)-ternary disordered structure], the change in DOS is in such a way that E_F falls in the real gap like in the Co_{Al} antisite-disordered structures, resulting in 100% P, whereas in the Mn-deficient structure [or the ($Co_{Mn} + Al_{Mn}$)-ternary antisite-disordered structure], the minority spin states at E_F get intensified compared with the ideal structure, leading to the reduction in P.

For further exploring the origin of observed changes in the DOS (and hence in P) of disordered structures, particularly the emergence of new states in SP valley, the partial DOS (PDOS) for the substituted (or disordered or replaced) atoms and its surrounding atoms have been calculated. PDOS plots of disordered atom(s) in Fig. 3 (binary antisite) and Fig. 4 (ternary antisite) reveal that the major changes in DOS near E_F arise from the disordered atom(s), whereas the contributions from the rest of the atoms within the unit cell are small and can be neglected (PDOS for other atoms not shown). The difference in the PDOS of the substituted atom in the case of the disordered alloy and the parent alloy is due to the

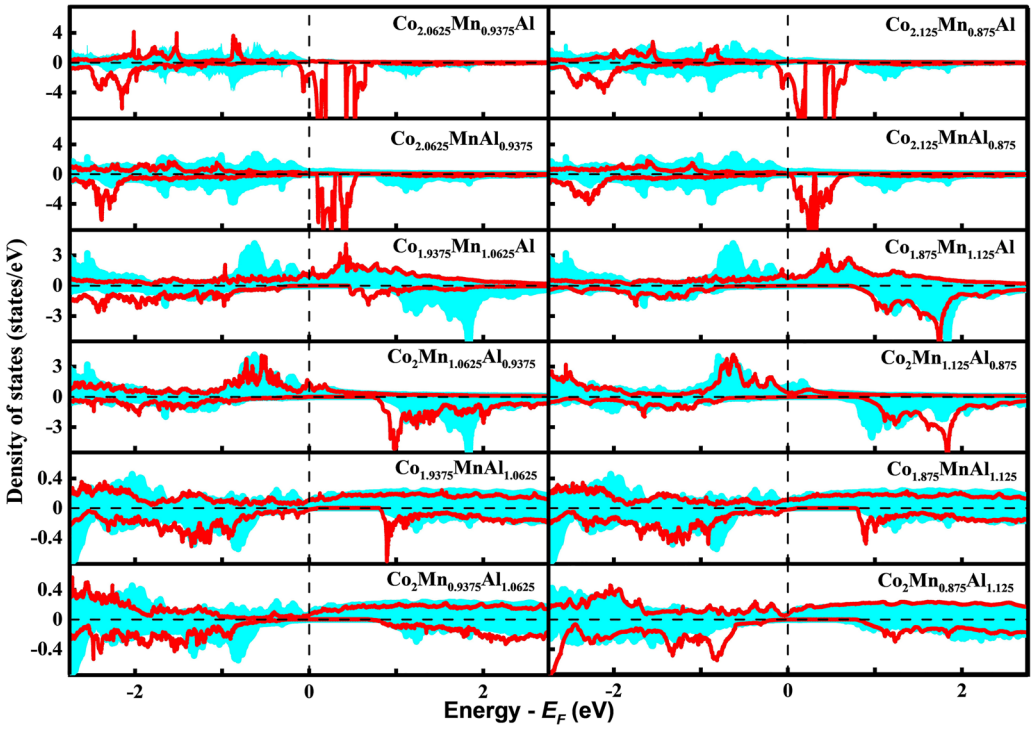

FIG. 3. Partial density of states (PDOS) plots for the disordered (substituted) atom in binary antisite disorders. The solid red lines represent the PDOS for the disorder atom, the shaded cyan area represents the PDOS for the corresponding atom in the ideal Co_2MnAl alloy. The corresponding stoichiometric formula for the disordered structure is given in the inset of each graph. It was found that, where two atoms were substituted, both substituted atoms had similar PDOSs; therefore, the PDOS for only one atom is shown here (since in the case of vacancy defects the atom is absent at the defect site, PDOS plots for vacancy defects are not provided).

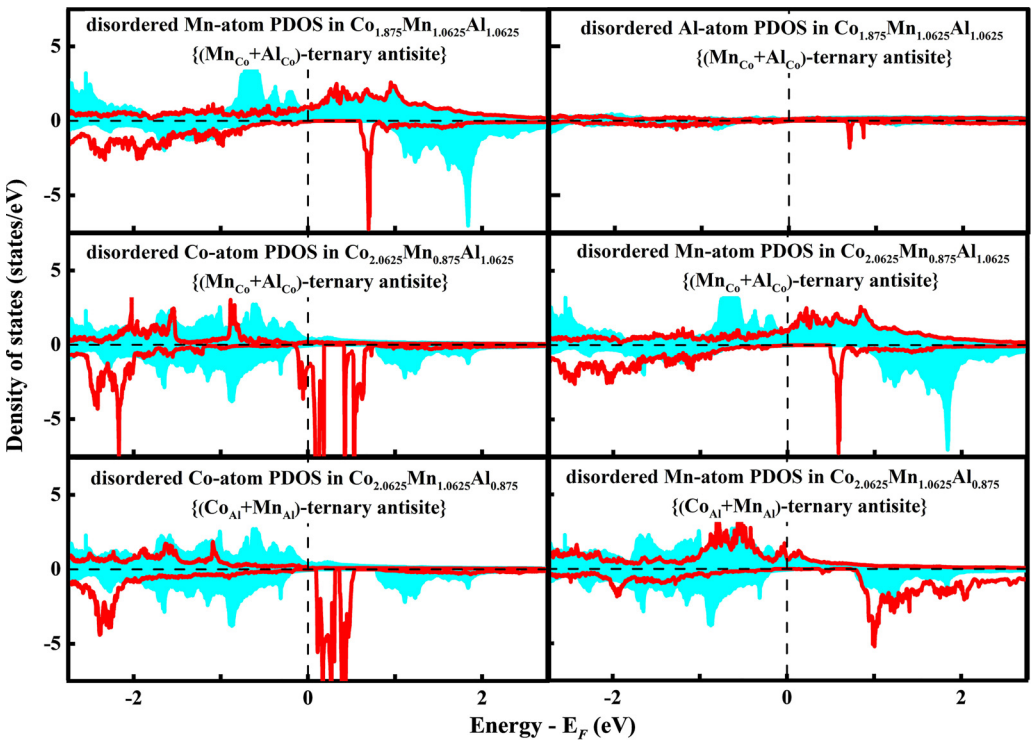

FIG. 4. Partial density of states (PDOS) plots for the disordered (substituted) atom in ternary antisite disorders. The solid red lines represent the PDOS for the disorder atom, the shaded cyan area represents the PDOS for the corresponding atom in the ideal Co_2MnAl alloy.

distinct symmetry at which they are situated in the disordered structure and ideal structure. Thus, it can be summarized that the effect of both binary and ternary antisite disorder on the electronic properties is localized in nature. However, PDOS plots for the vacancy-defected structures, like in Figs. 3 and 4, are not possible due to the absence of atoms at defect sites. For their analysis, PDOS plots from the other atoms in the defected structures have been utilized (not shown for brevity). In the vacancy-defected structures, the changes in PDOS were found to survive for several neighbors of vacancy sites or almost spread throughout the unit cell. Thus, vacancy defects lead to changes in hybridization up to next-nearest neighbors and, therefore, have long-range effects on the electronics properties. Such a long-range effect causes the electronic properties of the disordered alloy to be vulnerable to variations in vacancy defect concentrations.

Finally, let us compare these findings with the available results in Refs. [26,27]. As stated in the introduction section, Ref. [27] discussed the pseudogap, minority states across E_F, and P for the Co_{Mn}, Mn_{Co}, Mn_{Al}, and Al_{Mn} antisite-disordered structures at different disorder concentrations (quantified). In Ref. [26], the authors reported the effect of Al_{Mn}, Mn_{Al}, and Mn_{Co} antisite disorders and V_{Co}, V_{Mn}, and V_{Al} vacancy defects on the pseudogap and minority states across E_F; however, they did not provide the spin polarization values. Our results for the changes in P and minority states across E_F with disorder concentrations for binary antisite-disordered structures closely resemble the trends seen in the limited data from Refs. [26,27]. The slight disparities in the results can be attributed to variations in the supercell size and differences in the stoichiometric formula. However, in the case of vacancy defects, our results concerning the alterations in minority DOS differ from the observations in Ref. [26], which reveal that Co vacancies strongly affect the minority states, whereas Mn vacancies have a moderate effect. Conversely, present findings indicate that Mn vacancies have the most substantial effect, while Co vacancies yield a moderate influence. This disparity in the results may be ascribed to several factors, such as the nonlocalized nature of the impact of vacancy defects, slight variations in the stoichiometric formula, and differences in the calculation methods. The findings reported in Ref. [26] were computed using the full-potential local-orbital method with LDA for the XC, along with the coherent potential approximation method to simulate disorder randomly.

3. *Effect of point defects on magnetic properties of* Co_2MnAl

After that, we will discuss the magnetic moment of disordered structures. Recall that Co_2MnAl, in the bulk phase ($L2_1$-ordered structure), possesses a total magnetic moment of $4.02\,\mu_B$/f.u., equivalently a magnetic moment of $64.32\,\mu_B$ in the 64 atom supercell. As the defected structures are modeled using a 64 atom supercell, which is also the smallest unit cell for point defects, the total moment for the $L2_1$-ordered structure and various disordered structures is described using the 64 atom cell. For the disordered structures, the stoichiometric formula, total magnetic moment, atomic moment of the disordered atom(s), and estimated total magnetic moment as per the SP rule are gathered in Tables IV and V [53]. The total magnetic moment as per the SP rule is estimated using the formula ($Z - 16 \times 24$), where Z is the total valence electrons in a 64 atom supercell. The compositional formula for the disordered structures is also provided for reference. It is important to note that the SP rule is most accurate for perfect half-metallic HAs. For nearly half-metallic HAs, it provides a reasonably close estimate.

The total magnetic moment of the disordered structures exhibits slight deviations from the total moment of ideal structure, as illustrated in Tables IV and V. The extent of these deviations depends upon the specific disorder present in the sample, like in the case of P. Recognize that the total magnetic moment for an electronic structure is given by $\mu_B \times$ (number of spin-up electrons − number of spin-down electrons). Since in the context of disordered structures the substitution of atoms induces a change in the number of total valence electrons, a change in the total magnetic moment is also expected. Also, as the valence electron count changes due to the substituted atoms, the atomic magnetic moment is expected to be changed only for these specific atoms from the corresponding moments of the ideal atoms. However, it is found that the neighboring atoms of the substituted atoms also experience variations in their magnetic moments, and this phenomenon is specific to the type of disorder present. To gain deeper insight into the magnetic moments for other atoms, the local magnetic moment for all atoms within the 64 atom supercell has been mapped as the distance from disorder atoms in Figs. S2(a)–S2(r) and S3(a)–S3(c) in the Supplemental Material [35]. These figures clearly represent the variations in atomic magnetic moments within the unit cell. These changes in the atomic magnetic moments can be attributed to the changes in exchange splitting resulting from changes in hybridization. In the following, the magnetic moments for the different studied point defects, along with their concentrations, are presented.

For the binary antisite disorders with $x = 0.0625$, Al-poor structures resulting from binary antisite disorder (Co_{Al} and Mn_{Al} antisite disorders) show the increased total magnetic moment, whereas the Al-rich structure (resulting from Al_{Mn} antisite disorder) shows decreased magnetic moment. The rest of the disordered structures, viz., containing Mn_{Co}, Al_{Co}, and Co_{Mn} antisite disorder, have mild effects on the total magnetic moment, and the total magnetic moment remains nearly unchanged for them. The substantial changes in the total magnetic moment for disordered structures containing Co_{Al}, Mn_{Al}, and Al_{Mn} antisite disorders are due to the significant difference in valence electron count for the dopant and host atoms. Notably, Co, Mn, and Al have 9, 7, and 3 valence electrons, respectively (according to the pseudopotential configurations used for calculations). Based upon the valence electrons count, similar behavior should also be observed for the Al_{Co} disordered structure, i.e., decreased total magnetic moment compared with the ideal structure. However, the small increments in the atomic magnetic moments (AMMs) of several neighboring atoms accumulate and thus yield a total magnetic moment close to that of the ideal structure, as seen in Figs. S2(j) and S2(k) in the Supplemental Material [35]. Furthermore, it can also be observed from Fig. S2 in the Supplemental Material [35] that, for all considered binary antisite disorders, the AMMs at regular sites are barely changed or undergo negligible small change. This observation

TABLE IV. The different binary antisite and vacancy disordered structures and their total magnetic moments (calculated and as per the SP rule), and magnetic moments for disordered atom(s). X_d denotes the magnetic moment for the substituted atom(s).

Disorder structure	x	Composition formula	Total magnetic moment (μ_B/cell)		Magnetic moment for substituted atom(s), X_d (μ_B)
			Calculated	SP rule	
$L2_1$-ordered structure		$Co_{32}Mn_{16}Al_{16}$	64.32	64	–
		(Co_2MnAl)			
Co_{Mn} antisite disorder	0.0625	$Co_{33}Mn_{15}Al_{16}$	65.46	66	Co: 1.93
($Co_{2+x}Mn_{1-x}Al$)		($Co_{2.0625}Mn_{0.9375}Al$)			
	0.1250	$Co_{34}Mn_{14}Al_{16}$	66.74	68	Co: 1.93
		($Co_{2.125}Mn_{0.875}Al$)			Co: 1.93
Co_{Al} antisite disorder	0.0625	$Co_{33}Mn_{16}Al_{15}$	70.00	70	Co: 2.07
($Co_{2+x}MnAl_{1-x}$)		($Co_{2.0625}MnAl_{0.9375}$)			
	0.1250	$Co_{34}Mn_{16}Al_{14}$	76.00	76	Co: 2.08
		($Co_{2.125}MnAl_{0.875}$)			Co: 2.08
Mn_{Co} antisite disorder	0.0625	$Co_{31}Mn_{17}Al_{16}$	62.11	62	Mn: −2.09
($Co_{2-x}Mn_{1+x}Al$)		($Co_{1.9375}Mn_{1.0625}Al$)			
	0.1250	$Co_{30}Mn_{18}Al_{16}$	60.08	60	Mn: −2.09
		($Co_{1.875}Mn_{1.125}Al$)			Mn: −2.09
Mn_{Al} antisite disorder	0.0625	$Co_{32}Mn_{17}Al_{15}$	68.00	68	Mn: 2.45
($Co_2Mn_{1+x}Al_{1-x}$)		($Co_2Mn_{1.0625}Al_{0.9375}$)			
	0.1250	$Co_{32}Mn_{18}Al_{14}$	72.00	72	Mn: 2.42
		($Co_2Mn_{1.125}Al_{0.875}$)			Mn: 2.42
Al_{Co} antisite disorder	0.0625	$Co_{31}Mn_{16}Al_{17}$	64.44	58	Al: −0.05
($Co_{2-x}MnAl_{1+x}$)		($Co_{1.9375}MnAl_{1.0625}$)			
	0.1250	$Co_{30}Mn_{16}Al_{18}$	64.89	52	Al: −0.05
		($Co_{1.875}MnAl_{1.125}$)			Al: −0.05
Al_{Mn} antisite disorder	0.0625	$Co_{32}Mn_{15}Al_{17}$	60.24	60	Al: −0.05
($Co_2Mn_{1-x}Al_{1+x}$)		($Co_2Mn_{0.9375}Al_{1.0625}$)			
	0.1250	$Co_{32}Mn_{14}Al_{18}$	56.71	56	Al: −0.04
		($Co_2Mn_{0.875}Al_{1.125}$)			Al: −0.04
Co vacancy	0.0625	$Co_{31}Mn_{16}Al_{16}$	63.15	55	–
($Co_{2-x}MnAl$)		($Co_{1.9375}MnAl$)			
	0.1250	$Co_{30}Mn_{16}Al_{16}$	63.32	46	–
		($Co_{1.875}MnAl$)			
Mn vacancy	0.0625	$Co_{32}Mn_{15}Al_{16}$	59.33	57	–
($Co_2Mn_{1-x}Al$)		($Co_2Mn_{0.9375}Al$)			
	0.1250	$Co_{32}Mn_{14}Al_{16}$	55.99	50	–
		($Co_2Mn_{0.875}Al$)			
Al vacancy	0.0625	$Co_{32}Mn_{16}Al_{15}$	61.26	61	–
(Co_2MnAl_{1-x})		($Co_2MnAl_{0.9375}$)			
	0.1250	$Co_{32}Mn_{16}Al_{14}$	58.35	58	–
		($Co_2MnAl_{0.875}$)			

indicates that the influence of antisite disorder on the magnetic properties is localized in nature.

For the binary antisite-disordered structures corresponding to $x = 0.125$, owing to the considerable far distance between the substituted atoms in the disordered structures and the localized nature of binary antisite disorder with $x = 0.0625$ (for the magnetic moments), the magnetic moment for the disordered structures changes in a similar manner as in the case of binary antisite-disordered structures with $x = 0.0625$, and changes are amplified in the proportion of the disorder

TABLE V. Same as Table IV but here for ternary antisite-disordered structures.

Disorder type	x	Composition formula	Total magnetic moment (μ_B/cell)		Magnetic moment for substituted atom(s), X_d (μ_B)
			Calculated	SP rule	
$Mn_{Co} + Al_{Co}$	0.0625	$Co_{30}Mn_{17}Al_{17}$	62.19	56	Mn: −2.12
$(Co_{2-2x}Mn_{1+x}Al_{1+x})$		$(Co_{1.875}Mn_{1.0625}Al_{1.0625})$			Al: −0.03
$Co_{Mn} + Al_{Mn}$	0.0625	$Co_{33}Mn_{14}Al_{17}$	61.56	62	Co: 1.93
$(Co_{2+x}Mn_{1-2x}Al_{1+x})$		$(Co_{2.0625}Mn_{0.875}Al_{1.0625})$			Al: −0.05
$Co_{Al} + Mn_{Al}$	0.0625	$Co_{33}Mn_{17}Al_{14}$	74.00	74	Co: 2.07
$(Co_{2+x}Mn_{1+x}Al_{1-2x})$		$(Co_{2.0625}Mn_{1.0625}Al_{0.875})$			Mn: 2.49

concentration (i.e., nearly doubled). Also, the effect of disorder on magnetic moments remained localized, as illustrated in Figs. S2(a)–S2(l) in the Supplemental Material [35]. The calculated magnetic moment values for Co_{Mn}, Mn_{Al}, and Al_{Mn} antisite-disordered structures are closely aligned and exhibit a similar trend with a change in disorder concentration (i.e., change in a similar way), with the results reported in Refs. [26,27] wherever possible. This alignment validates our findings and can be attributed to the localized nature of antisite defects, which lead to comparable outcomes despite having nearly identical stoichiometric formulas. Further, any minute differences observed can be attributed to slight variations in the stoichiometric compositions considered in Refs. [26,27].

For the vacancy defects with $x = 0.0625$, corresponding to the monovacancies, the absence of an atom within the lattice leads to a notable decrease in the total magnetic moment. This decrement is evident, as the absence of an atom leads to a reduction in the total valence count. Furthermore, as illustrated in Figs. S2(m)–S2(r) in the Supplemental Material [35], unlike the case of the binary antisite disorders, the AMM map for the vacancy-defected structures is complicated in nature, and neighboring atoms also make significant contributions to change in total magnetic moment. As a result, the calculated magnetic moment values for the vacancy-defected structures differ significantly from the SP rule. The most substantial changes occur in the presence of V_{Mn} and V_{Al}, where the magnetic moment decreases significantly. In contrast, the presence of V_{Co} has a marginal effect on the total magnetic moment, leaving it nearly the same as the ideal structure. For the vacancy defects, considerable fluctuations in the magnetic moments of distant neighboring atoms indicate that the vacancy defects have a nonlocalized effect on the AMMs. Because of this nonlocalized nature (or long-range survival) of the vacancy-defect impact, the change in the magnetic moments happens arbitrarily on increasing vacancy defects concentration (i.e., with $x = 0.125$ or for the divacancies). As observed in Figs. S2(m)–S2(r) in the Supplemental Material [35], the alterations in AMMs extend to sixth nearest neighbors for Co monovacancy, up to the third nearest neighbors for Mn monovacancy, and up to the second nearest neighbors for Al monovacancy. In the scenario of divacancies (i.e., with $x = 0.125$), these effects reach out to the fourth, fourth, and second nearest neighbors for the divacancies of Co, Mn, and Al atoms, respectively.

Finally, in the case of the ternary antisite disorders, the total magnetic moment of the Co-deficient structure [(Mn_{Co} + Al_{Co})-ternary antisite] and Mn-deficient structure [(Co_{Mn} + Al_{Mn})-ternary antisite] is nearly identical to the magnetic moment of the ideal structure due to almost the same valence electrons, whereas the Al-deficient structure [resulting from ($Co_{Al} + Mn_{Al}$)-ternary antisite] exhibits an increased magnetic moment due to the significant alternations in valence electrons count. For all considered ternary antisite disorders, the impact of the disorder on magnetic properties is also localized, like binary antisite disorders, as demonstrated in Figs. S3(a)–S3(c) in the Supplemental Material [35].

Hence, within the context of point defects, to conclude overall, it can be stated that both binary and ternary antisite disorders result in localized alterations in AMMs, whereas the vacancy defects lead to complex change in AMMs, which is very sensitive to their concentrations. This behavior resembles that observed for electronic properties (spin polarization) and is also expected since both are linked to the PDOS. Thus, based on the magnetic moment and DOS analysis (Sec. III B 2), it can be inferred that point defects act as a minor perturbation in the case of antisite disorder, whether binary or ternary, but it is notable when it comes to vacancy defects.

Another noteworthy observation in the overall picture is that the SP rule is followed by the disordered structures having 100% polarization, viz., Al-deficient structure from binary and ternary antisite disorder [Co_{Al} and Mn_{Al} binary antisite structures, and ($Co_{Al} + Mn_{Al}$)-ternary antisite structure; c.f. Tables IV and V]. This reaffirms the half-metallicity of these disordered structures, as discussed in Sec. III B 2. Additionally, for the remaining disordered structures, the total magnetic moment closely corresponds to the predictions of the SP rule, except in the case of Al_{Co} antisite disorder and vacancy defects. For Al_{Co} disorder, small positive contributions from neighboring atoms in the disordered structure yield a total magnetic moment that closely resembles that of the ideal structure, as discussed earlier. In vacancy defects, deviations from the SP rule can be ascribed to the alterations in AMMs throughout the unit cell, originating from the nonlocalized nature of vacancy defect impacts.

Notably, the most interesting changes were observed in the Co-deficient structures originating from Mn_{Co} binary antisite disorder and ($Mn_{Co} + Al_{Co}$)-ternary antisite disorder, irrespective of disorder concentration. The presence of the Mn_{Co} antisite among these structures induces the antiferromagnetic

coupling between the AMM of the antisite-Mn atom and neighboring ideal atoms (Co and Mn). Since these disordered structures also possess very high P (as shown in Tables II and III), it can be concluded that the creation of the Mn_{Co} antisite leads to half-metallic antiferrimagnetism (HMFi), which is highly desirable for spintronics applications. This beautiful phenomenon has also been theoretically observed for many other HAs, like Co_2CrSi [26], Co_2MnSi [26,49], Co_2CrAl [26,54], Co_2VSn [55], Ti_2CoAl [56], Ti_2FeAl [57], and Ti_2NiAl [58], where the presence of Y_X antisite disorders lead to the antiferromagnetic coupling between the doped atom and ideal atoms. Thus, creation of Y_X antisite disorder (within X_2YZ HAs) could be an alternative promising way to make HMFi, and its further experimental investigations could be interesting.

In summary, the present calculations for the spin polarization and total magnetic moment (Secs. III B 2 and III B 3) for different disordered structures of Co_2MnAl alloy collectively suggest that there is no straightforward rule that connects the electronic and magnetic properties to the disorder. Instead, this depends on the disorder-induced specific changes in electronic structure, which is different for different HAs.

C. Effect of lattice distortions on structural, electronic, and magnetic properties of Co_2MnAl

In this section, we present DFT results on the effect of lattice distortions by considering uniform compressive strain, uniform tensile strain, and tetragonal distortions on structural, electronic, and magnetic properties of Co_2MnAl using a 4 f.u. unit cell (i.e., 16 atom supercell). For modeling the uniform strain, the lattice parameter (a) is uniformly contracted and expanded by varying the volume of the cubic unit cell from $V_0 - 10\%V_0$ to $V_0 + 10\%V_0$, in 21 steps with step size of $1\%V_0$. Here, V_0 represents the volume corresponding to the fully relaxed cubic structure (or $L2_1$-ordered structure) and is calculated as $V_0 = (a_0)^3$, where a_0 is the optimized lattice parameter for $L2_1$-ordered Co_2MnAl (5.69 Å). The uniform strain is defined as percent change in optimized volume, i.e., $\Delta V/V_0$ ($\times 100\%$) with $\Delta V = (V - V_0)$. This uniform strain leads to lattice parameters ranging from 5.50 to 5.88 Å. For tetragonal distortions, three different volumes for the tetragonal unit cell are considered (viz., V_0 and $V_0 \pm 5\%V_0$). The tetragonal distortion is then modeled at each volume with cell parameters $a = b$ and $0.5 \leqslant c/a \leqslant 1.5$. Here, tetragonal distortion can be defined in terms of $\Delta c/a$, i.e., variation of the c/a value from 1.00. For the tetragonally distorted cell with volume V_0, lattice parameters range between $4.97\,\text{Å} \leqslant a \leqslant 7.17\,\text{Å}$ and $3.59\,\text{Å} \leqslant c \leqslant 7.46\,\text{Å}$, whereas for the tetragonal distorted cell with volume $V_0 - 5\%$ ($V_0 + 5\%$), the lattice parameter changes between $4.88\,\text{Å} \leqslant a \leqslant 7.05\,\text{Å}$ ($5.05\,\text{Å} \leqslant a \leqslant 7.29\,\text{Å}$) and $3.52\,\text{Å} \leqslant c \leqslant 7.33\,\text{Å}$ ($3.64\,\text{Å} \leqslant c \leqslant 7.58\,\text{Å}$). Tables S1–S4 in the Supplemental Material [35] depict the lattice parameters for the cubic strained and tetragonally distorted structures.

The range for lattice distortion, as mentioned above, is considered using the following factors: The experimental lattice parameter for cubic HAs is generally 1–2% larger than the theoretically calculated lattice parameter, resulting from the heat treatment during the experiments or stress from growth technique such as sputtering [21]. Moreover, within the HA heterostructures, the lattice mismatch with the adjacent layers generally leads to a change in the lattice parameter of HA by 2–3%. All these alternations in the lattice parameter are approximately equivalent to a maximum volume change of $\sim \pm 10\%$ in the optimized value. Therefore, volume change of $\pm 10\%$ has been considered by varying the unit-cell volume uniformly to model uniform strain.

For modeling the tetragonal distortion, three different volume values V_0, ($V_0 + 5\%V_0$), and ($V_0 - 5\%V_0$) are considered for the tetragonal unit-cell volume, and then at each of these volumes, the c/a value is varied from 0.5 to 1.5 for modeling the tetragonal unit cells. The choice of the tetragonal unit cell volume as V_0 or with slightly varied volume ($V_0 \pm 5\%V_0$) is based upon the observation that most of the technologically important full cubic HAs with stable or metastable tetragonal phase often exhibit the same volume as in their cubic phase or show minor changes. For example, in the tetragonally distorted Co-, Fe-, and Mn-based full HAs with high PMA, the volume change is of the order of 1–5% (with $1.2 \leqslant c/a \leqslant 1.4$) between stable cubic and tetragonal phases [59,60]; numerous all-d-metal-based HAs (particularly Mn-Ni-V based) exhibit stable tetragonal structure with the same equilibrium volume as their cubic structure with $1.42 \leqslant c/a \leqslant 1.44$, and in many ferromagnetic shape memory alloys, the volume for the equilibrium state does not change under tetragonal distortion [61]. Meanwhile, the extremes of these distortions are chosen at relatively high values to study the trends in the results. In the following subsections, the effect of uniform strain and tetragonal distortions will be discussed in detail.

1. *Effect of uniform strain on structural, electronic, and magnetic properties of* Co_2MnAl

The RFE for the lattice distorted structures (with respect to $L2_1$-ordered structure) have been calculated, like for the point-defected structures in Sec. III B 1. In the case of lattice-distorted structures, the last term in Eq. (1) does not exist, as the total number of atoms in the lattice distorted structure is the same as that of the ideal $L2_1$ structure. Accordingly, the RFE for the lattice-distorted structures, sometimes termed as the distortion formation energy, is given by

$$E_{\text{form}}(A) = E(A) - E(O), \tag{3}$$

where $E_{\text{form}}(A)$, $E(A)$, and $E(O)$ are the RFE of the lattice distorted structure, total energies of the lattice-distorted structure (A), and total energies of the equivalent-sized relaxed cubic structure ($L2_1$), respectively. The effects of uniform cubic strain (or a variation) on the structural, electronic, and magnetic properties are summarized in Fig. 5. All uniformly strained structures have positive RFE, as Fig. 5(a) depicts. With increasing the uniform strain values ($\Delta V/V_0$), the RFE increases in a parabolic way, emerging from the change in the potential energy of the strained structures.

The positive RFE for the uniformly strained structures suggests that the growth of uniformly strained structures is relatively less favorable during the formation of the Co_2MnAl alloy, as compared with the $L2_1$-ordered structure. However, for a considerably wide range of cubic strain, corresponding

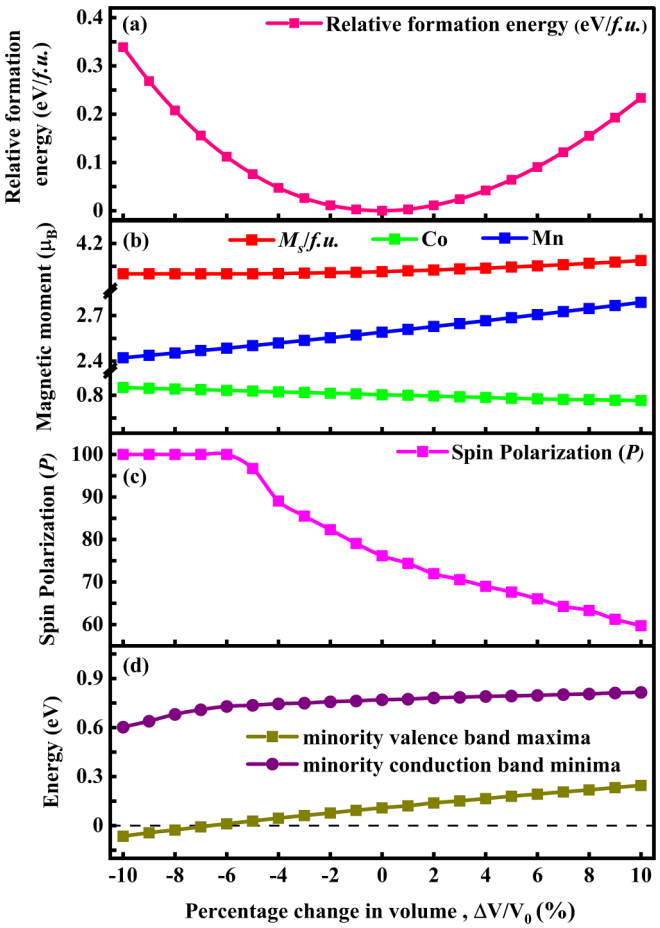

FIG. 5. (a) Relative formation energy, (b) total and atomic magnetic moments, (c) spin polarization, and (d) minority valence band maxima and minority conduction band minima for uniformly (or isotropically) strained Co_2MnAl alloy as a function of percent change in unit-cell volume ($\Delta V/V_0 = \{V - V_0\}/V_0$). The horizontal short-dashed line in (d) indicates the Fermi level.

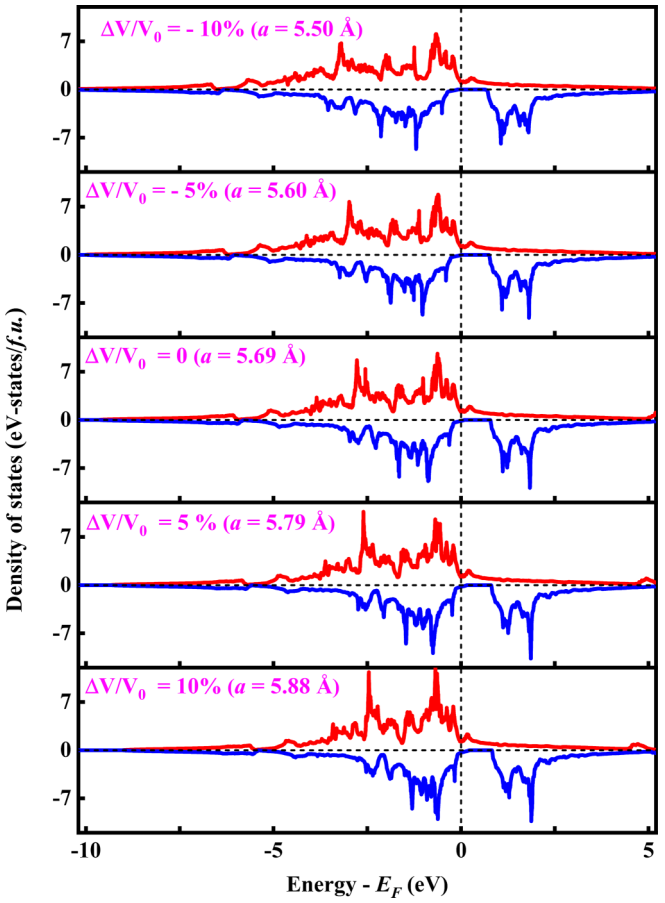

FIG. 6. Density of states (DOS) plots for −10%, −5%, 0%, 5%, and 10% ($\Delta V_0/V_0$) uniformly strained Co_2MnAl alloy. The red and blue solid lines show the majority and minority DOSs.

to $-5\% \leqslant \Delta V/V_0 \leqslant 6\%$, the RFE for the uniformly strained structure is <0.1 eV/f.u. This is comparable with the thermal energy typically encountered during experiments and meets the criteria for distortion formation energy for most of the experimentally observed strained structures for full HAs. Thus, it can be inferred that, during the growth of Co_2MnAl, the uniformly (or isotropically) strained structure with volume $0.95V_0 \leqslant V \leqslant 1.06V_0$ (equivalent to the lattice parameter ranging between 5.60 and 5.81 Å) should be easily formed in experiments. Beyond that, the occurrence probability for the strained structure decreases rapidly with $|\Delta V/V_0|$ due to the sharp increase of distortion formation energy.

Thereafter, the effect of strain on electronic properties was investigated using DOS. The spin-polarized DOS plots under uniform strain are shown in Fig. 6, where we present DOS only for few strain values, viz., $\Delta V/V_0 = 0, \pm 5$, and $\pm 10\%$. The Fermi energy is shifted to zero in Fig. 6. Under the uniform strain, there are minor changes in the minority spin DOS near E_F, while the majority spin DOS remains nearly the same as for the relaxed structure. The general shape of DOS for the uniformly strained structure did not change due to the similar crystallography to the relaxed structure. For the negative strain ($\Delta V/V_0 \leqslant 0$), the smaller unit-cell volume of the strained structure results in the broader and shallower bands because of the increased electronic orbitals overlapping, as illustrated in Figs. 6(a) and 6(b). The opposite effect is observed with positive strain ($\Delta V/V_0 \geqslant 0$) due to the increased localization, and the strained structure exhibits narrower and peakier bands, as seen in Figs. 6(c) and 6(d). Apart from these minute changes in DOS shape, some other minor changes in DOS for uniformly strained structures include change in the minority energy gap width ($E_{gap} = E_c - E_v$) and shifting in the Fermi level (or equivalently to change in the gap center $\{(E_c + E_v)/2\}$ or shifting of minority energy band with respect to E_F). All these changes are somewhat similar to what were observed in point-defect cases, such as all changes happening in the minority DOS only. As seen from Fig. 5(d), E_{gap} decreased with increasing the cell volume and changed from 0.67 to 0.57 eV at extreme of strain [62]. As for the free-electron gas, E_F changes with unit-cell volume as $E_F \propto V^{-2/3}$; therefore, for the uniformly strained structures, change in E_F with unit-cell volume is also expected (Fig. S4(a) in the Supplemental Material [35]). Other factors influencing E_F and E_{gap} under uniform strain include changes in the electronic localization and exchange coupling, as depicted in PDOS

plots, also explained for Co_2MnGe, Co_2CrAl, and Co_2FeAl alloys in the literature [13,22,23].

The trends in minority valence band maxima, minority conduction band minima, P, atomic magnetic moments, and total magnetic moments for the cubic strained structures are given in Figs. 5(b)–5(d). For the negative strains (or uniform compressive strain), Co_2MnAl possesses enhanced P along with 100% polarization for the strain values up to $\Delta V/V_0 \leqslant -6\%$. Above that, as the strain values increase beyond 7%, P decreases monotonically with increasing strain value (i.e., increasing unit-cell volume); however, it remains high, reaching $\sim 60\%$ at $\Delta V/V_0 = 10\%$ ($a = 5.88$ Å). The primary reason for the change in P is the shifting of E_F in the minority spin channel. Here, E_F is pinned in the valley in the majority spin channel, and the shifting occurs only independently in the minority spin channel, like in the case of point defects. At extreme negative strain, E_F is situated in the energy gap, resulting in perfect half-metallic nature for the strained structure. With increasing positive strain, E_F shifts toward the minority valence band. As a result, for $(\Delta V/V_0) > -6\%$, P decreases linearly for uniformly strained structures while increasing the cell volume.

The total magnetic moment remains nearly constant for all investigated strain values. Specifically, for strain values up to $\Delta V/V_0 \leqslant -6\%$, M_s is an integer (i.e., 4.00 μ_B/f.u.). This is consistent with the SP rule for half-metallic full HAs (i.e., integer magnetic moments for HAs with 100% P). For other strain values ($\Delta V/V_0 > -6\%$), negligible changes in M_s were observed at second decimal points. Concerning the AMM, when the lattice expands, Co and Mn atoms go toward a more isolated atomlike situation due to the increased localization (or because of reduced hybridization within the d states). This increased localization for Co and Mn atoms with increasing cell volume is also evident by the enhanced peaky and narrow bands in their PDOSs (Fig. S5 in the Supplemental Material [35]). As a result, due to increased localization, the Mn magnetic moment increases with increased cell volume [63,64]. In contrast, the Co AMM shows the opposite trend and decreases with positive strain. However, the rate of change for the Co AMM with respect to strain value is very small compared with the rate of change for the Mn AMM, which is attributed to the more itinerant nature of the Co atom than the Mn atom. Thus, the increment in the Mn AMM is compensated for the Co AMM and interstitial moments, leaving the total spin moment constant, as in the case of the ideal structure across all strain values. Generally, the change in the Co AMM in Co-based HAs with strain predominantly depends upon the specific Y-type atom (in X_2YZ HAs), whereas for the Y-type atom, the AMM always increases with increasing uniform strain. For example, in the Co_2MnSi and Co_2CrAl alloys, the Co AMM decreases with increasing positive strain, while it increases in the Co_2FeAl alloy. Therefore, these findings regarding the trend in the change in AMMs are consistent with that of other Co-based HAs. Also, in terms of spin polarization and total magnetization, the effect of uniform strain is found to be like that observed in the case of other full HAs, like Co_2MnSb [12], Co_2MnGe [13], Co_2CrAl [22], and Co_2FeAl [23]. In summary, it can be deduced that uniform strain has minimal impact on M_s, while P changes significantly, depending upon the strain value.

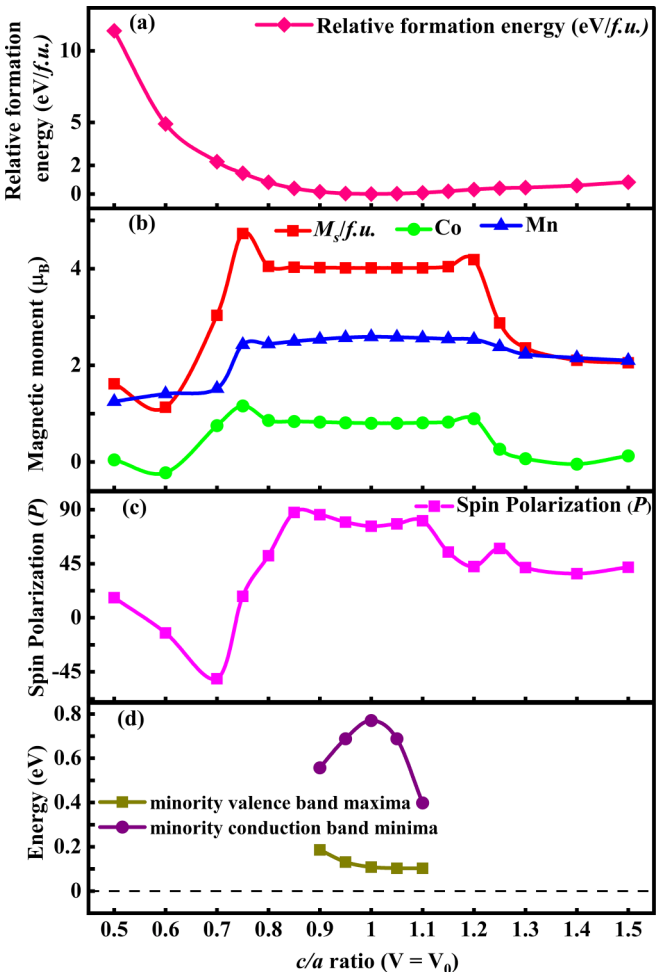

FIG. 7. (a) Relative formation energy, (b) total and atomic magnetic moments, (c) spin polarization, and (d) minority-spin valence band maxima and conduction band minima as a function of c/a value for tetragonal structures with V_0 unit-cell volume. The horizontal short-dashed line in (d) indicates the Fermi level.

2. *Effect of tetragonal distortions on structural, electronic, and magnetic properties of* Co_2MnAl

As mentioned in the introduction section, tetragonal distortion is anticipated in thin films and is helpful for many practical technological applications. Therefore, this section will discuss the effect of tetragonal distortion on the structural, electronic, and magnetic properties of the Co_2MnAl alloy. Figures 7–10 present the structural, electronic, and magnetic properties of tetragonally distorted structures, at different c/a values, with $V = V_0$, $(V_0 - 5\%V_0)$, and $(V_0 + 5\%V_0)$ volumes, respectively. Based on the calculated RFE as presented in Figs. 7(a), 9(a), and 10(a), it is evident that the tetragonally deformed structures have very high positive RFE, which increases with increasing $|\Delta c/a|$ values. Therefore, the tetragonally distorted structures are less likely to be formed (or relatively less favored for formation) than the $L2_1$-ordered structure.

However, the tetragonally distorted structures with V_0 volume, for very small distortion values ranging between $c/a = 0.95$ and 1.10, have low RFE $\leqslant 0.1$ eV/f.u., making

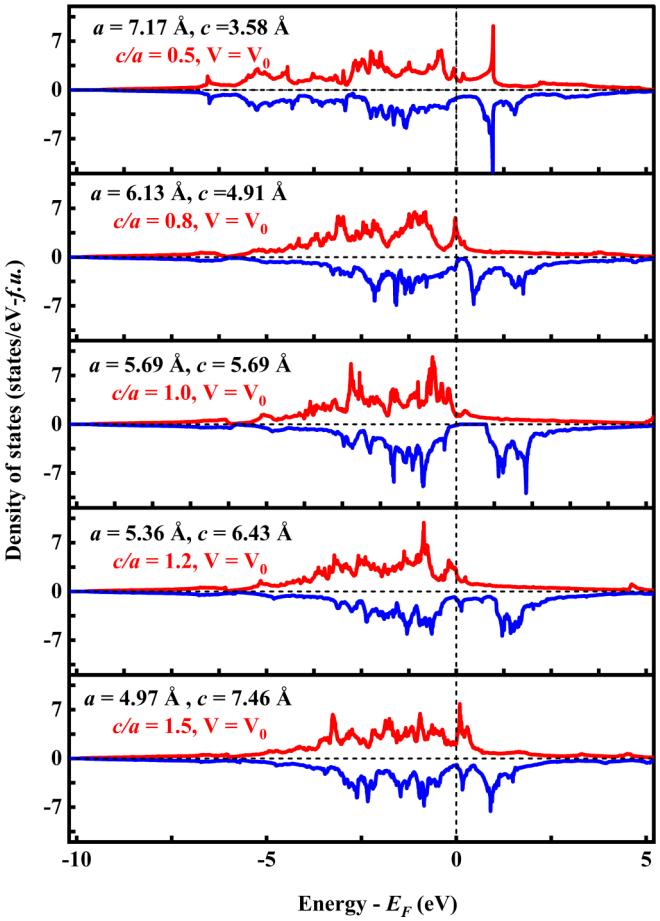

FIG. 8. Density of states (DOS) plots for tetragonally distorted structures with $c/a = 0.5$, 0.8, 1.0, 1.2, and 1.5 with V_0 unit-cell volume. The red and blue solid lines show the majority and minority DOSs.

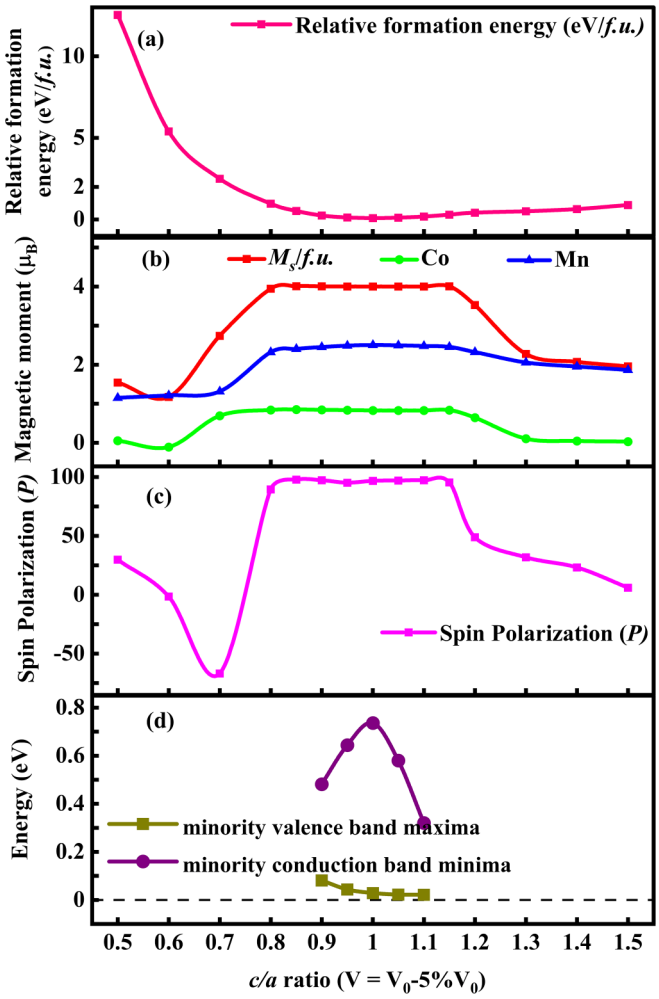

FIG. 9. Same as Fig. 7 but here for the tetragonal structures with $(V_0 - 5\%V_0)$ unit-cell volume.

their occurrence highly probable. Beyond these c/a values, RFE increases rapidly with increasing $|\Delta c/a|$ values, making their occurrence probability decrease with increasing $|\Delta c/a|$ values. As seen from Figs. 9(a) and 10(a), a similar trend is observed for tetragonally distorted structures with $(V_0 \pm 5\%V_0)$ volumes, except for the c/a values with RFE $\leqslant 0.1$ eV/f.u. For the tetragonally distorted structures with $(V_0 + 5\%V_0)$ volumes, this c/a range changes between 0.95 and 1.10, whereas for the tetragonally distorted structures with $(V_0 + 5\%V_0)$ volumes have RFE $\geqslant 0.1$ eV/f.u. for all considered c/a values.

Also, for all c/a values, tetragonal structures with compressed volume (i.e., $V = V_0 - 5\%V_0$) have the highest RFE, followed by the tetragonal distorted structure with increased volume (i.e., $V = V_0 + 5\%V_0$). In contrast, those with V_0 volume have the lowest RFE. At a particular c/a value, the change in the RFE with respect to tetragonal unit-cell volume can be attributed to the change in potential energy of the tetragonal structure with respect to unit-cell volume. Therefore, among the V_0 and $(V_0 \pm 5\%)$ volumes, tetragonal distortion is most likely to occur with the V_0 volume. This explains why most full HAs have identical volumes in the tetragonal and cubic phases. Another significant point to note about the RFE of the tetragonally distorted structures is that RFE is much larger for the compression along the c axis (with elongation of the ab plane) than the elongation along the c axis (with compression of the ab plane), regardless of their volume. Thus, it is concluded that the favored condition for tetragonal distortion is elongation along the c axis (with compression of the ab plane).

Following that, let us discuss DOS and P for the tetragonally distorted structures. For the tetragonally distorted structures, the DOS undergoes significant alterations due to the weight redistribution, resulting from the reduced symmetry of the crystal structure. Consequently, the principal features of HA band structure, i.e., peak and valley characteristics, disappear, and a broader and shallow DOS compared with the optimized cubic structure is observed. This phenomenon is easily noticeable in the DOS plot as depicted in Fig. 8, which shows the DOS plot for the tetragonal structures with V_0 volume and different c/a values. For the tetragonally distorted structures, as far as the c/a value deviates from 1.0, the DOS becomes more smoothly distributed and dispersive. However, the DOS remained relatively unaltered for minimal distortion values (i.e., for very small $|\Delta c/a|$ values, around 1.0), depending upon deformed unit-cell volume.

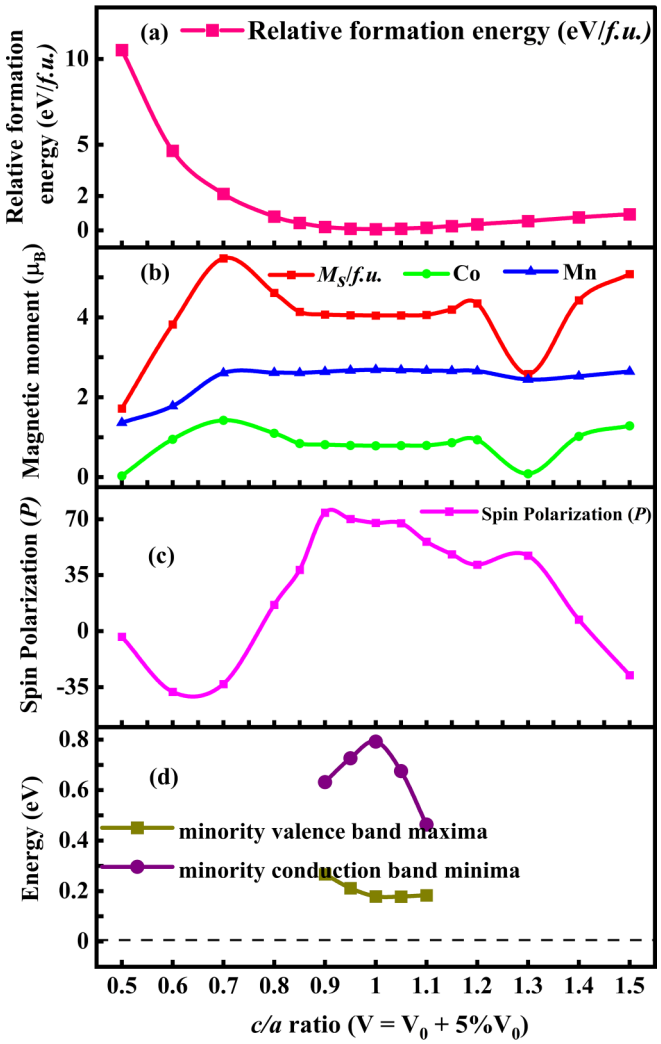

FIG. 10. Same as Fig. 7 but here for the tetragonal structures with $(V_0 + 5\%V_0)$ unit-cell volume.

For the tetragonally deformed structures with V_0 volume, with very small distortion values ($0.85 \leqslant c/a \leqslant 1.10$), the DOS shape is nearly the same as in case of the $L2_1$-ordered structure with an intact SP valley (not shown). This leads to a nearly half-metallic behavior for them, along with very high spin polarization like the $L2_1$-ordered structure. Further large distortion (i.e., higher $|\Delta c/a|$ values) results in the closing of the SP valley due to the large overlapping of the atomic orbitals along the contraction direction. Therefore, a dominating metallic nature with a considerable reduction in P is observed for the remaining deformed structures (i.e., with $c/a \leqslant 0.85$ and $c/a \geqslant 1.10$), as seen in Fig. 7(c). Specifically, as c/a values increased from 1.10, P declined almost monotonically, reaching 42% at $c/a = 1.5$. Conversely, when the c/a value decreased from 0.85, P showed a random drop, and it even changed its sign at $c/a = 0.7$ and 0.6 with P values of -50% and -12%, respectively. Here, the primary influence on P for the tetragonally distorted structures arises from the altered shape of the DOS. Unlike the case of the uniformly strained structures, the shift in the Fermi level is not as significant as for the tetragonally distorted structures due to the simultaneous elongation and contraction while maintaining the constant unit-cell volume (V_0 here) in the tetragonally distorted unit cell (see Fig. S4(b) in the Supplemental Material [35]). Therefore, the shifting of E_F has negligible contribution in the alternation in P, like in the case of uniform strain. For the tetragonal distorted structures with altered unit-cell volume ($V_0 - 5\%V_0$ and $V_0 + 5\%V_0$), the DOS as well as P follow nearly the same pattern as for the tetragonally structures with V_0 volume. However, the SP valley or the minority spin gap was found to be presented over a slightly wider range of c/a (from 0.80 to 1.15) for the tetragonally distorted cell with decreased volume as compared with structures with increased volume (from 0.90 to 1.10) and structures with optimized volume (from 0.85 to 1.10), as indicated by Figs. 7(d), 9(b), and 10(d).

Furthermore, at a particular c/a value, the distorted structures with decreased volume ($V_0 - 5\%V_0$) maintain the high spin polarization values compared with distorted structures having V_0 and ($V_0 + 5\%V_0$) volume, as seen in Figs. 7(c), 9(c), and 10(c). The structures with ($V_0 + 5\%V_0$) volume have the lowest P. For the tetragonally deformed structures, at a particular c/a value, the decline in P with increasing the unit-cell volume (from $V_0 - 5\%V_0$ to $V_0 + 5\%V_0$) can be attributed to the weakening covalent hybridization on increasing the cell volume [23]. Thus, for P of tetragonally distorted cells, it can be summarized that P changes arbitrarily and shows nonmonotonic behavior with c/a values, which primarily originates from the altered shape of the DOS including the closing of the minority energy gap or the SP valley. Also, for small distortion, the deformed structures maintain high P and the minority spin gap, and the large distortion (large $|\Delta c/a|$ value) results in reduced P. For a particular c/a value, P decreased on increasing the cell volume.

The total magnetic moment also follows a similar trend as P, i.e., for the small deviation of the c/a value from 1.0, distorted structures have nearly the same moment values as the $L2_1$-ordered structure, whereas large deviations of c/a from 1.0 lead to a significant alternation in magnetic moment values [Figs. 7(b), 9(b), and 10(b)]. For $0.80 \leqslant c/a \leqslant 1.15$, the total magnetic moment is nearly the same as in the case of relaxed cubic structure ($\sim 4\,\mu_B$/f.u.) for the tetragonally distorted structure with V_0 volume. The corresponding ranges for ($V_0 - 5\%V_0$) and ($V_0 + 5\%V_0$) volume distorted cells are $0.85 \leqslant c/a \leqslant 1.15$ and $0.90 \leqslant c/a \leqslant 1.10$, respectively. For further large $|\Delta c/a|$ values, change in hybridization primarily resulting from the change in nearest neighbors causes significantly different magnetic moment values, regardless to their volume. In addition to Figs. 7, 9, and 10, RFE, magnetic moments, and spin polarization for tetragonal distorted structures with V_0 and ($V_0 \pm 5\%V_0$) volumes are also tabulated in Tables S4–S6 in the Supplemental Material [35] for better comprehension.

Finally, we discuss the structural stability for the tetragonally distorted Co_2MnAl alloy. Recall that the RFE also provides information relative to thermodynamic stability of the defected structures, in addition to the ease of occurrence of the disorder. As the tetragonally distorted structures have very high positive RFE, as observed from Figs. 7(a), 9(a), and 10(a), the tetragonally distorted structures for the Co_2MnAl HA are relatively less stable compared with the

ordered cubic structure. The reason behind this instability of the tetragonally distorted Co_2MnAl lies in its electronic configurations and can be attributed to the higher valence band energies for the tetragonal structures in comparison with the relaxed cubic structure. The valence band energy for the relaxed cubic structure or the tetragonally distorted structure can be written as $E_{\text{band}} = \int_{E=E_v}^{E_F} dE\text{DOS}(E)E$, as discussed in Ref. [25]. Compared with the relaxed cubic structure, the tetragonally deformed structures have higher DOS near E_F (see Figs. 6 and 8). Hence, for the tetragonally distorted structure, in the conjugation with the number of valence electrons $N_v = \int_{E=E_v}^{E_F} dE\text{DOS}(E)$, the increased DOS around E_F leads to the higher band energies for the tetragonal structures. However, the absence of a metastable or stable tetragonal phase for Co_2MnAl in this paper may also be limited due to the constrained volume approach and/or the shuffling of atoms in a larger and big supercell for making the tetragonal cell and therefore require further study [65].

IV. CONCLUSIONS

The signature of structural imperfections is frequently observed in the HAs like a perturbation to the ordered structure, which strongly affects their physical properties. Given that Co_2MnAl has been reported to exhibit some exceptional properties in the presence of point defects and lattice distortions, such as appearance of SGS nature, emergence of PMA, and enhanced spin polarization, along with partial availability of results for the effect of point defects and lattice distortions, a detailed study of the effect of various point defects (binary antisite disorder, ternary antisite disorder, and vacancy defects) and the lattice distortions (uniform cubic strains and tetragonal distortions) on the structural, electronic, and magnetic properties of the technologically important HA Co_2MnAl has been done explicitly for uncovering some remarkable results. While the point defect is considered up to a maximum disorder concentration of 12.50% using a 64 atom supercell, cubic strain ($\Delta V/V_0$) is simulated within the range of $\pm 10\%$ ($5.50\,\text{Å} \leqslant a \leqslant 5.88\,\text{Å}$) using a 16 atom supercell, and tetragonal deformation is modeled by varying the c/a value between 0.5 and 1.5 at three different unit-cell volumes V_0 and ($V_0 \pm 5\%V_0$) using a 16 atom supercell.

The Mn-deficient structures resulting from Al_{Mn} binary antisite disorder ($Co_2Mn_{0.9375}Al_{1.0625}$ and $Co_2Mn_{0.875}Al_{1.125}$) and from ($Co_{Mn} + Al_{Mn}$)-ternary antisite disorder ($Co_{2.0625}Mn_{0.875}Al_{1.0625}$) exhibit negative RFEs with respect to the $L2_1$-ordered structure; therefore, they could spontaneously occur during the growth of the Co_2MnAl alloy. The Co_{Al} antisite-disordered structures ($Co_{2.0625}MnAl_{0.9375}$ and $Co_{2.125}MnAl_{0.875}$), the ($Co_{Al} + Mn_{Al}$) antisite-disordered structure ($Co_{2.0625}Mn_{1.0625}Al_{0.875}$), and monovacancy- and divacancy-defected structures for Co, Mn, and Al atomic sites have very high positive RFEs with respect to the $L2_1$-ordered structure, which make their occurrence unlikely, or they are expected to have very small density. The Co_{Al} binary antisite-disordered structures ($Co_{2.0625}MnAl_{0.9375}$ and $Co_{2.125}MnAl_{0.875}$), Mn_{Al} binary antisite-disordered structures ($Co_2Mn_{1.0625}Al_{0.9375}$ and $Co_2Mn_{1.125}Al_{0.875}$), and ($Co_{Al} + Mn_{Al}$)-ternary antisite-disordered structures ($Co_{2.0625}Mn_{0.875}Al_{1.0625}$) exhibit perfect half-metallicity, i.e., 100% spin polarization and integer magnetic moment according to the SP rule. The rest of the antisite disorders have marginal effect on half-metallic properties of Co_2MnAl, and the disordered structures maintain high spin polarization ($\geqslant 70\%$) along with the nearly constant magnetization as for $L2_1$-ordered structure. Furthermore, emergence of the half-metallic ferrimagnetism phenomenon in the Mn_{Co} binary antisite and ($Mn_{Co} + Al_{Co}$)-ternary antisite-disordered structures (namely, $Co_{1.9375}Mn_{1.0625}Al$, $Co_{1.875}Mn_{1.125}Al$, and $Co_{1.875}Mn_{1.0625}Al_{1.0625}$), resulting from the antiparallel orientation between the atomic moments of the disordered atom and neighboring transition metal elements, suggests a possible method for synthesizing the half-metallic ferrimagnetic material and requires further experimental investigations. For all considered antisite-disordered structures (binary as well as ternary), analyses of the PDOS and atomic magnetic moments show that disordered (substituted) atoms are solely owing for the changes in the spin polarization and magnetization of Co_2MnAl; therefore, the effect of the disorder on electronic and magnetic properties is localized in nature. However, unlike the case of antisite disorders, the vacancy defects significantly affect the electronic and magnetic properties of Co_2MnAl. They were found to alter the pseudogap strongly, including the complete shrinking of Co and Mn vacancies. Another contrasting feature of vacancy defects is that their impact extends to several neighbors; consequently, electronic and magnetic properties are very susceptible to their concentrations.

For the lattice distortions, the uniform strain ranging between $-5\% \leqslant \Delta V/V_0 \leqslant 6\%$ is most probable to be found in the real sample due to their low RFEs with respect to the $L2_1$-ordered structure. Also, due to the same crystal structure, the DOS remains unaltered under the uniform (isotropic) strain. However, the shifting of E_F in the minority spin channel causes the appearance of half-metallicity for $-10\% \leqslant \Delta V/V_0 \leqslant -7\%$ (corresponding to $5.50\,\text{Å} \leqslant a \leqslant 5.56\,\text{Å}$). Beyond $\Delta V/V_0 \geqslant -6\%$, spin polarization decreases monotonically with the increase in the positive strain, dropping to $\sim 60\%$ at $\Delta V/V_0 = +10\%$ ($a = 5.88\,\text{Å}$). The total magnetic moment for all uniformly strained structures is nearly the same as the $L2_1$-ordered structure.

On the other hand, for the tetragonally distorted structures, except for small distortion values (within $c/a \sim 0.9 - 1.1$), they have very high RFEs for all considered c/a values and unit-cell volumes (V_0 and $V_0 \pm 5\%V_0$). Therefore, tetragonal distortion is less probable to occur than the ordered structure. Moreover, the elongation along the c axis (with compression of the ab plane) with V_0 volume is the favored condition for the occurrence of tetragonal distortion over the compression along the c axis (with elongation of the ab plane). The high spin polarization and minority spin pseudogap for the tetragonally distorted structures are found to be kept only for very small deviation of the c/a value from 1.0, notably for $0.85 \leqslant c/a \leqslant 1.10$ at V_0 volume, for $0.80 \leqslant c/a \leqslant 1.15$ at ($V_0 - 5\%V_0$) volume, for $0.90 \leqslant c/a \leqslant 1.10$ at ($V_0 + 5\%V_0$) volume. However, more substantial deviations in the c/a value lead to significant changes in the DOS shape, including the closing of the pseudogap, resulting in the change in spin polarization and magnetic moment in an arbitrary way.

In this paper, we show that, while some structural imperfections (binary antisite disorder, ternary antisite disorder, and uniform strain) could be beneficial for Co_2MnAl from the spintronics point of view, some others (vacancy defects and tetragonal distortions) could have adverse effects and therefore should be avoided by carefully selecting the substrates or insertion of spacer layers and/or by controlling the growth mechanism. We believe that this paper would be useful for experimentalists to form high-quality thin films as desired in spintronic devices. We did not find any stable or metastable noncubic structure for Co_2MnAl. The other possible volume of the tetragonally deformed cell and other possible high-symmetric lattice deformations, like octahedral distortion, should also be studied for the search of stable or metastable noncubic structure for Co_2MnAl. Also, the study of the disordered structures combining the antisite disorder and lattice distortions is a subject worthy of further investigation.

ACKNOWLEDGMENTS

The authors would like to thank the IIT Delhi HPC facility for computational resources. A.K. acknowledges the Council of Scientific and Industrial Research (Grant No. 09/086(1356)/2019-EMR-I) India for the senior research fellowship. The authors thank M. Ali Haider, B. K. Mani, S. Bhattacharya, and R. S. Dhaka of IIT Delhi, and Manish Kumar, School of Physical Science, JNU Delhi, for helpful discussions.

[1] Y. Miura, M. Shirai, and K. Nagao, *Ab initio* study on stability of half-metallic Co-based full-Heusler alloys, J. Appl. Phys. **99**, 08J112 (2006).

[2] H. C. Kandpal, G. H. Fecher, and C. Felser, Calculated electronic and magnetic properties of the half-metallic, transition metal based Heusler compounds, J Phys D Appl Phys **40**, 1507 (2007).

[3] M. Jourdan, J. Minár, J. Braun, A. Kronenberg, S. Chadov, B. Balke, A. Gloskovskii, M. Kolbe, H. J. Elmers, G. Schönhense *et al.*, Direct observation of half-metallicity in the Heusler compound Co_2MnSi, Nat. Commun. **5**, 3974 (2014).

[4] G. K. Shukla, A. K. Jena, N. Shahi, K. K. Dubey, I. Rajput, S. Baral, K. Yadav, K. Mukherjee, A. Lakhani, K. Carva *et al.*, Atomic disorder and berry phase driven anomalous Hall effect in a Co_2FeAl Heusler compound, Phys. Rev. B **105**, 035124 (2022).

[5] P. J. Webster and K. R. A. Ziebeck, Magnetic and chemical order in Heusler alloys containing cobalt and titanium, J. Phys. Chem. Solids **34**, 1647 (1973).

[6] S. Singh, R. Rawat, S. E. Muthu, S. W. D'Souza, E. Suard, A. Senyshyn, S. Banik, P. Rajput, S. Bhardwaj, A. M. Awasthi *et al.*, Spin-valve-like magnetoresistance in Mn_2NiGa at room temperature, Phys. Rev. Lett. **109**, 246601 (2012).

[7] P. Chen, Z. Yan, X. Liu, D. Cao, D. Gao, and C. Gao, Tetragonal distortion modified magnetism and anomalous Hall effect of Mn_2CoAl Heusler alloys through Ar ion irradiation, J. Phys. D Appl. Phys. **55**, 475001 (2022).

[8] K. Seema, The effect of pressure and disorder on half-metallicity of CoRuFeSi quaternary Heusler alloy, Intermetallics **110**, 106478 (2019).

[9] D. Rani, J. Kangsabanik, K. G. Suresh, N. Patra, D. Bhattacharyya, S. N. Jha, and A. Alam, Origin of local atomic order and disorder in $Co_2Fe_{1-x}Cr_xSi$ Heusler alloys: Theory and experiment, Phys. Rev. Appl. **10**, 054022 (2018).

[10] S. Gupta, S. Chakraborty, V. Bhasin, S. Pakhira, S. Dan, C. Barreteau, J.-C. Crivello, S. N. Jha, M. Avdeev, J.-M. Greneche *et al.*, High spin polarization in the disordered quaternary Heusler alloy FeMnVGa, Phys. Rev. B **108**, 045137 (2023).

[11] Enamullah, D. D. Johnson, K. G. Suresh, and A. Alam, Half-metallic Co-based quaternary Heusler alloys for spintronics: Defect- and pressure-induced transitions and properties, Phys. Rev. B **94**, 184102 (2016).

[12] Enamullah and S.-C. Lee, High-efficient and defect tolerant Co_2MnSb ternary Heusler alloy for spintronic application, J. Alloys Compd. **765**, 1055 (2018).

[13] M. J. Carey, T. Block, and B. A. Gurney, Band-structure calculations of imperfect Co_2MnGe Heusler compounds, Appl. Phys. Lett. **85**, 4442 (2004).

[14] M. Rostami, Half-metallic property of the bulk and (001) surfaces of MNaCs (M = P, As) half-Heusler alloys: A density functional theory approach, Surf. Sci. **674**, 103 (2018).

[15] M. S. Gabor, T. Petrisor, C. Tiusan, M. Hehn, and T. Petrisor, Magnetic and structural anisotropies of Co_2FeAl Heusler alloy epitaxial thin films, Phys. Rev. B **84**, 134413 (2011).

[16] V. Barwal, S. Hait, N. K. Gupta, L. Pandey, V. Mishra, A. Kumar, N. Kumar, N. Sharma, R. K. Meena, and S. Chaudhary, Effect of stoichiometry and film thickness on the structural and magnetization dynamics behavior of Co_2MnAl thin films cosputtered on Si(100), J. Magn. Magn. Mater. **552**, 169246 (2022).

[17] S. Hait, S. Husain, V. Barwal, N. K. Gupta, L. Pandey, P. Svedlindh, and S. Chaudhary, Comparison of high temperature growth versus post-deposition *in situ* annealing in attaining very low Gilbert damping in sputtered Co_2FeAl Heusler alloy films, J. Magn. Magn. Mater. **519**, 167509 (2021).

[18] V. Mishra, A. Kumar, L. Pandey, N. K. Gupta, S. Hait, V. Barwal, N. Sharma, N. Kumar, S. Chandra, and S. Chaudhary, Disordered spin gapless semiconducting CoFeCrGa Heusler alloy thin films on Si (100): Experiment and theory, Nanoscale **15**, 337 (2022).

[19] E. Chason, M. Karlson, J. J. Colin, D. Magnfält, K. Sarakinos, and G. Abadias, A kinetic model for stress generation in thin films grown from energetic vapor fluxes, J. Appl. Phys. **119**, 145307 (2016).

[20] T. J. Vink, M. A. J. Somers, J. L. C. Daams, and A. G. Dirks, Stress, strain, and microstructure of sputter-deposited Mo thin films, J. Appl. Phys. **70**, 4301 (1991).

[21] G. Abadias, E. Chason, J. Keckes, M. Sebastiani, G. B. Thompson, E. Barthel, G. L. Doll, C. E. Murray, C. H. Stoessel, and L. Martinu, Review article: Stress in thin films and coatings:

Current status, challenges, and prospects, J. Vac. Sci. Technol. A **36**, 020801 (2018).

[22] T. Block, M. J. Carey, B. A. Gurney, and O. Jepsen, Band-structure calculations of the half-metallic ferromagnetism and structural stability of full- and half-Heusler phases, Phys. Rev. B **70**, 205114 (2004).

[23] A. Ahmad, S. K. Srivastava, and A. K. Das, Phase stability and the effect of lattice distortions on electronic properties and half-metallic ferromagnetism of Co_2FeAl Heusler alloy: An *ab initio* study, J. Phys.: Condens. Matter **32**, 415606 (2020).

[24] Y. Liu, L. Ren, Y. Zheng, S. He, Y. Liu, P. Yang, H. Yang, and K. L. Teo, Doping effects on structural and magnetic properties of Heusler alloys $Fe_2Cr_{1-x}Co_xSi$, AIP Adv. **8**, 056328 (2018).

[25] C. Felser, L. Wollmann, S. Chadov, G. H. Fecher, and S. S. P. Parkin, Basics and prospective of magnetic Heusler compounds, APL Mater. **3**, 041518 (2015).

[26] I. Galanakis, K. Özdoğan, and E. Şaşioğlu, Role of defects and disorder in the half-metallic full-Heusler compounds, in *Advances in Nanoscale Magnetism*, Springer Proceedings in Physics, edited by B. Aktas and F. Mikailov (Springer, Berlin, 2009), Vol. 122.

[27] Y. Feng, T. Zhou, X. Chen, H. Yuan, and H. Chen, The effect of Mn content on magnetism and half-metallicity of off-stoichiometric Co_2MnAl, J. Magn. Magn. Mater. **387**, 118 (2015).

[28] V. Barwal, N. Behera, S. Husain, N. K. Gupta, S. Hait, L. Pandey, V. Mishra, and S. Chaudhary, Spin gapless semiconducting behavior in inverse Heusler $Mn_{2-x}Co_{1+x}Al$ ($0 \leqslant x \leqslant 1.75$) thin films, J. Magn. Magn. Mater. **518**, 167404 (2021).

[29] S. Nepal, R. Dhakal, and I. Galanakis, *Ab initio* study of the half-metallic full-Heusler compounds Co_2ZAl [Z = Sc, Ti, V, Cr, Mn, Fe]; the role of electronic correlations, Mater. Today Commun. **25**, 101498 (2020).

[30] A. Kumar, V. Barwal, R. K. Meena, S. Chaudhary, and S. Chandra, B2-disorder effects on the structural, electronic and magnetic properties of Co_2MnAl Heusler alloy, J. Magn. Magn. Mater. **563**, 169871 (2022).

[31] Z. F. Yu, J. Lu, H. L. Wang, X. P. Zhao, D. H. Wei, J. L. Ma, S. W. Mao, and J. H. Zhao, Tunable perpendicular magnetic anisotropy in off-stoichiometric full-Heusler alloy Co_2MnAl, Chin. Phys. Lett. **36**, 067502 (2019).

[32] P. Giannozzi, S. Baroni, N. Bonini, M. Calandra, R. Car, C. Cavazzoni, D. Ceresoli, G. L. Chiarotti, M. Cococcioni, I. Dabo *et al.*, QUANTUM ESPRESSO: A modular and open-source software project for quantum simulations of materials, J. Phys.: Condens. Matter **21**, 395502 (2009).

[33] P. Giannozzi, O. Andreussi, T. Brumme, O. Bunau, M. B. Nardelli, M. Calandra, R. Car, C. Cavazzoni, D. Ceresoli, M. Cococcioni *et al.*, Advanced capabilities for materials modelling with QUANTUM ESPRESSO, J. Phys.: Condens. Matter **29**, 465901 (2017).

[34] M. Cococcioni and S. De Gironcoli, Linear response approach to the calculation of the effective interaction parameters in the LDA + U method, Phys. Rev. B **71**, 035105 (2005).

[35] See Supplemental Material at http://link.aps.org/supplemental/10.1103/PhysRevMaterials.8.034405 for DOS plots for $L2_1$-ordered Co_2MnAl, using GGA and GGA + U methods. For the point defected structures (namely, binary antisite disorders, ternary antisite disorders, and vacancy defects), Fermi energy and atomic magnetic moments maps are also given to support the main text related to the effect of point defects on various physical properties of Co_2MnAl. Moreover, lattice parameter(s), RFE, spin polarization, total magnetic moment, atomic magnetic moment, Fermi energy, and partial DOS for uniformly strained and tetragonally distorted structures are also included, which includes Refs. [66,67] therein.

[36] E. Şaşioğlu, I. Galanakis, C. Friedrich, and S. Blügel, *Ab initio* calculation of the effective on-site Coulomb interaction parameters for half-metallic magnets, Phys. Rev. B **88**, 134402 (2013).

[37] C. Tsirogiannis and I. Galanakis, Effect of the double-counting functional on the electronic and magnetic properties of half-metallic magnets using the GGA + U method, J. Magn. Magn. Mater. **393**, 297 (2015).

[38] P. J. Webster, Magnetic and chemical order in Heusler alloys containing cobalt and manganese, J. Phys. Chem. Solids **32**, 1221 (1971).

[39] C. Guillemard, W. Zhang, G. Malinowski, C. de Melo, J. Gorchon, S. Petit-Watelot, J. Ghanbaja, S. Mangin, P. Le Fèvre, F. Bertran *et al.*, Engineering $Co_2MnAl_xSi_{1-x}$ Heusler compounds as a model system to correlate spin polarization, intrinsic Gilbert damping, and ultrafast demagnetization, Adv. Mater. **32**, 1908357 (2020).

[40] L. Makinistian and E. A. Albanesi, Electronic and magnetic properties of the Co_2MnAl/Au interface: Relevance of the Heusler alloy termination, J. Magn. Magn. Mater. **385**, 133 (2015).

[41] S. J. Ahmed, C. Boyer, and M. Niewczas, Magnetic and structural properties of Co_2MnSi based Heusler compound, J. Alloys Compd. **781**, 216 (2019).

[42] V. V. Sokolovskiy, M. E. Gruner, P. Entel, M. Acet, A. Çakır, D. R. Baigutlin, and V. D. Buchelnikov, Segregation tendency of Heusler alloys, Phys. Rev. Mater. **3**, 084413 (2019).

[43] Energy Dispersive X-ray Spectroscopy Services, EAG Laboratories, www.eag.com/techniques/spectroscopy/energy-dispersive-x-ray-spectroscopy-eds/.

[44] M. P. Raphael, B. Ravel, Q. Huang, M. A. Willard, S. F. Cheng, B. N. Das, R. M. Stroud, K. M. Bussmann, J. H. Claassen, and V. G. Harris, Presence of antisite disorder and its characterization in the predicted half-metal Co_2MnSi, Phys. Rev. B **66**, 104429 (2002).

[45] T. Graf, G. H. Fecher, J. Barth, J. Winterlik, and C. Felser, Electronic structure and transport properties of the Heusler compound Co_2TiAl, J. Phys. D Appl. Phys. **42**, 084003 (2009).

[46] M. Wójcik, E. Jedryka, H. Sukegawa, T. Nakatani, and K. Inomata, ^{59}Co NMR experiment as a probe of electron doping in $Co_2FeAl_{1-x}Si_x$ Heusler alloys, Phys. Rev. B **85**, 100401(R) (2012).

[47] C. G. Van De Walle and J. Neugebauer, First-principles calculations for defects and impurities: Applications to III-nitrides, J. Appl. Phys. **95**, 3851 (2004).

[48] S. Picozzi, A. Continenza, and A. J. Freeman, Role of structural defects on the half-metallic character of Co_2MnGe and Co_2MnSi Heusler alloys, Phys. Rev. B **69**, 094423 (2004).

[49] B. Hülsen, M. Scheffler, and P. Kratzer, Thermodynamics of the Heusler alloy $Co_{2-x}Mn_{1+x}Si$: A combined density functional theory and cluster expansion study, Phys. Rev. B **79**, 094407 (2009).

[50] S. V. Malik, E. T. Dias, A. K. Nigam, and K. R. Priolkar, Antisite disorder and phase segregation in Mn_2NiSn, J. Phys. D Appl. Phys. **55**, 165002 (2022).

[51] S. V. Malik, E. T. Dias, V. Srihari, P. D. Babu, and K. R. Priolkar, Role of antisite disorder in the martensitic transition of $Ni_{2-x}Mn_{1+x}Ga$, Intermetallics **148**, 107613 (2022).

[52] S. V. Faleev, Y. Ferrante, J. Jeong, M. G. Samant, B. Jones, and S. S. P. Parkin, Origin of the tetragonal ground state of Heusler compounds, Phys. Rev. Appl. **7**, 034022 (2017).

[53] I. Galanakis, P. H. Dederichs, and N. Papanikolaou, Slater-pauling behavior and origin of the half-metallicity of the full-Heusler alloys, Phys. Rev. B **66**, 174429 (2002).

[54] B. Abu Alhaj and B. Hamad, The effect of defects on the electronic and magnetic properties of Co_2CrAl Heusler alloy, J. Phys. Chem. Solids **74**, 265 (2013).

[55] N. T. Mahmoud, J. M. Khalifeh, B. A. Hamad, and A. A. Mousa, The effect of defects on the electronic and magnetic properties of the Co_2VSn full Heusler alloy: *Ab-initio* calculations, Intermetallics **33**, 33 (2013).

[56] Y. Chen, B. Wu, H. Yuan, Y. Feng, and H. Chen, The defect-induced changes of the electronic and magnetic properties in the inverse Heusler alloy Ti_2CoAl, J. Solid State Chem. **221**, 311 (2015).

[57] Q.-L. Fang, J.-M. Zhang, K.-W. Xu, and V. Ji, The effect of defects on the magnetic properties and spin polarization of Ti_2FeAl Heusler alloy, J. Magn. Magn. Mater. **351**, 25 (2014).

[58] Y. Zhou, Y. Chen, Y. Feng, H. Yuan, and H. Chen, First-principles study on the effect of defects on the electronic and magnetic properties of the Ti_2NiAl inverse Heusler alloy, Eur. Phys. J. B **87**, 290 (2014).

[59] Y. I. Matsushita, G. Madjarova, J. K. Dewhurst, S. Shallcross, C. Felser, S. Sharma, and E. K. U. Gross, Large magnetocrystalline anisotropy in tetragonally distorted Heuslers: A systematic study, J. Phys. D Appl. Phys. **50**, 095002 (2017).

[60] L. Wollmann, S. Chadov, J. Kübler, and C. Felser, Magnetism in tetragonal manganese-rich Heusler compounds, Phys. Rev. B **92**, 064417 (2015).

[61] J. G. Tan, Z. H. Liu, Y. J. Zhang, G. T. Li, H. G. Zhang, G. D. Liu, and X. Q. Ma, Site preference and tetragonal distortion of Heusler alloy Mn-Ni-V, Results Phys **12**, 1182 (2019).

[62] K. H. J. Buschow and F. R. de Boer, Itinerant-electron magnetism, in *Physics of Magnetism and Magnetic Materials* (Springer, Boston, 2003), pp. 63–73.

[63] I. Galanakis, P. H. Dederichs, and N. Papanikolaou, Origin and properties of the gap in the half-ferromagnetic Heusler alloys, Phys. Rev. B **66**, 134428 (2002).

[64] H. Luo, Z. Zhu, L. Ma, S. Xu, H. Liu, J. Qu, Y. Li, and G. Wu, Electronic structure and magnetic properties of Fe_2YSi (Y = Cr, Mn, Fe, Co, Ni) Heusler alloys: A theoretical and experimental study, J. Phys. D Appl. Phys. **40**, 7121 (2007).

[65] A. Ayuela, J. Enkovaara, K. Ullakko, and R. M. Nieminen, Structural properties of magnetic Heusler alloys, J. Phys.: Condens. Matter **11**, 2017 (1999).

[66] S. Han, C. S. Tang, L. Li, Y. Liu, H. Liu, J. Gou, J. Wu, D. Zhou, P. Yang, C. Diao *et al.*, Orbital-hybridization-driven charge density wave transition in CsV_3Sb_5 kagome superconductor, Adv. Mater. **35**, 2209010 (2023).

[67] B. Freelon, Y. Liu, Y. S. Liu, C. R. Rotundu, S. D. Wilson, J. H. Guo, J. Chen, W. Yang, C. L. Chang, P. A. Glans *et al.*, Electronic structure of $PrFeAsO_{1-\delta}$: An investigation using x-ray absorption and emission spectroscopy, J. Phys.: Conf. Ser. **273**, 012092 (2011).